May 2018

Temperature measurement in flames using TLAF, alkali emission and OH UV absorption

Yuhe Zhang

Division of Combustion Physics
Lund University

Master of Science Thesis

Temperature measurement in flames using TLAF, alkali emission and OH UV absorption

LUND
UNIVERSITY

Yuhe Zhang

Division of Combustion Physics

Department of Physics

This dissertation is submitted for the degree of

Master of Science

Lund University June 2018

Abstract

There is a continued need for reliable and convenient nonintrusive thermometric techniques for better understanding and effective control of combustion related processes. In this thesis, three spectroscopic thermometric methods were studied to evaluate the hot flue gas temperatures provided by a multi-jet burner. These methods include the two-line atomic fluorescence (TLAF) thermometry, the Na/K two-line emission method, and the thermometry using OH absorption spectroscopy. The temperature distribution along the long-side of the burner was measured using the TLAF method with an estimated uncertainty of $\pm$ 50 K. The emission intensity ratios between the Na 589 nm and the K 766 nm lines were investigated, which showed strong temperature dependence at lean flames with an excess oxygen content higher than 2.2%. The emission intensity ratios between the K 404 nm and 766 nm spectral lines were also investigated and found to be strongly dependent on the OH concentration instead of the temperature due to the effect of chemi-excitation. The feasibility of thermometry using OH absorption spectrum was studied by two spectral fitting methods: the direct fitting method and the second derivative fitting method. Both methods were able to evaluate the temperature within an accuracy of 60 K, while the latter method provided better accuracy due to the proper elimination of the baseline deviations. A comparison of the three thermometric methods was discussed in the end.

Table of contents

Abbreviations

CARS Coherent anti-Stokes Raman scattering

ECDL External cavity diode laser

HITRAN High-resolution transmission molecular absorption database

HWHM Half width at half maximum

ICCD Intensified charge-coupled device

LIF Laser-induced fluorescence

OH Hydroxyl

TDLAS Tunable diode laser absorption spectroscopy

TLAF Two-line atomic fluorescence

TMI Trimethylindium

UV Ultraviolet

Chapter 1

Introduction

Combustion processes have served human beings for thousands of years. More than 80 percent of the energy consumed nowadays in the world is provided by the combustion of fossil fuels leading to over 80 percent of total greenhouse emissions every day. To be specific, the combustion of fossil-fuel for the purposes of electricity, transportation, and industry produce more than 100 million metric tons of carbon dioxide (CO_2) everyday, i.e. 40 billion metric tons in a year, and the different greenhouse gases can remain in the atmosphere for a various amount of time ranging from several years to thousands of years. Although flame and fire are closely related to people's lives, there are still a great number of physical and chemical reactions that remain unknown regarding the detailed combustion processes. A better fundamental understanding of the combustion processes is needed with the rapidly increased demand for environmental protection, in order to control the combustion process more effective and clean.

Of many physical quantities concerned in combustion research, temperature is one of the most essential that describes the average heat or thermal energy of the particles in a substance; it is of great importance in the combustion process due to the distinct characters showing by reactants at different temperatures. Nearly all of the chemical reactions involving in the formation of pollutants and heat release show a strong dependence on temperature. In scientific research, temperature is important for validation of efficient flame simulations, e.g., the kinetic models of nitrogen oxides (NO_x) and soot formation under different conditions in laminar or turbulent flames. Additionally, since thermal stress determines the materials' reliability, and the lifetime of the combustion devices, reliable temperature measurements are essential for the investigation and realization of advanced combustion devices which can decrease the fuel consumption and reduce the pollutant production. Therefore, accurate and reliable information

of reaction temperature is indispensable for better understanding and control of combustion process.

1.1 Review of thermometry

Techniques of temperature measurement in combustion environment can be classified into three categories [1]. The first is intrusive measurement, which means the measuring devices contact directly with the gas medium of interest. Generally known instrumentation include thermocouple, thermometer, and resistance temperature devices. The temperature measured in an intrusive way is determined by the conductive, convective and radiative heat transfers between the sensor surface and its surroundings. For this reason, intrusive measurement instruments introduce a disturbance to the measured medium temperature, and the temperature obtained can be slightly different from that when the sensor is absent. The second category is semi-intrusive measurements, in which temperature sensitive materials are applied to the sample surface to enable remote observation, e.g., surface coatings by thermographic phosphors or thermochromic liquid crystals whose color changes with temperature. Although intrusive and semi-intrusive techniques provide valuable temperature information in some applications, to some extent perturbations are involved in the measurement. In contrast, nonintrusive measurements commonly conduct by probing atoms or molecules in the medium of interest with light while recording the electromagnetic spectra to obtain temperature information. One exception is acoustic thermometry, where the temperature is determined by measuring the speed of sound [2]. Nonintrusive measurements are often preferred to obtain accurate temperature. Optical-based techniques mostly derive temperature from the measured thermal population of selected atoms or molecules by using the Boltzmann distribution. This type of methods include coherent anti-Stokes Raman scattering (CARS) [3], a sophisticated thermometric technique with good accuracy and precision often regarded as a gold standard in laser diagnostics, laser-induced fluorescence (LIF) [4], degenerate four-wave mixing (DFWM) [5], two-line LIF (indium, gallium [6], hydroxyl (OH) [7], nitric oxide (NO) [8]), absorption spectroscopy and emission spectroscopy. An alternative way of obtaining temperature is to monitor the atomic and molecular spectral line width while the temperature can be deduced from the temperature-dependent Doppler and collisional broadening. This kind of techniques includes spontaneous Rayleigh and Raman scattering [9]. Most of the optical-based thermometric methods are based

on the development of modern photonic techniques. Lasers, fine optics and specialized data collection instruments are generally required, which sometimes makes the system complicated and highly expensive. Despite the advantages of each intrusive and nonintrusive techniques under certain conditions, there is still a high demand for reliable and convenient nonintrusive thermometric techniques for gas phase temperature measurement.

1.2 Novelties of this work

This thesis reports on the development of two inexpensive and easy-to-operate spectroscopic thermometric methods: two-line alkali emission method and thermometry based on OH absorption spectroscopy. The work involved in the thesis was conducted on a multi-jet burner [10] which is able to provide with variable oxygen concentration and homogeneous temperature ranging from 1000 K to 2500 K. Another thermometric method, two-line atomic fluorescence (TLAF), was also presented in the thesis. TLAF was firstly brought up by Alkemade [11] in the 1970s, and it has been further developed by numerous studies [12, 6] and proved to be a robust thermometric technique. A similar TLAF system as the one described in [13] was adopted in this work, which has been estimated to have an accuracy of 3% and a precision of 1% [13]. These results were used to validate the other two thermometric methods.

Alkali metals, especially sodium and potassium, show bright emissions in flames. Many studies have been conducted to investigate the temperature dependence of the light intensity emitted by alkali atoms in flames. Withrow et al. [14] firstly measured the hot gas temperature in internal combustion engines using the sodium-line reversal method with sodium chloride (NaCl) mist fuel additives in order to visualize the combustion process. Afterwards, Reissing et al. [15] creatively took advantage of the emission intensity ratios of sodium and potassium to estimate the hot gas temperature in a gasoline direct-injection engine, but they assumed that the emission intensity ratio of Na over K was only affected by the excited states population, and thus disregarded the concentration difference caused by chemical equilibrium between the atomic Na and K. The method was improved by Mosburger et al. [16] on a direct-injection research engine by adding lithium as a third alkali component to the flame and used the fluorescence ratio $Na{\cdot}Li/K^2$ as a marker of temperature. They took the concentration of atomic Na and K into consideration, and also quantitatively calculated the influence of self-absorption on the temperature measurement. The results given by Mosburger was promising where the

uncertainty was around ±100 K. A similar work has been conducted by the author [17] on a modified Perkin-Elmer burner, in which the temperature dependence of the fluorescence signal Na/K is acceptable, while that of Na·Li/K^2 is not interpretable. Nonetheless, the narrow adjustable temperature range (less than 100K) of the modified Perkin-Elmer burner was a notable limitation of the measurements. To counter this limitation, a novel multi-jet burner with controllable broader temperature range was used in this work. Additionally, in the previous work, the concentration of the alkali metal atoms in the gas region was just roughly calculated from theoretical simulation, which would introduce error. By contrast, the absorption spectroscopy was used in this thesis work to directly measure the concentration of K atoms, in order to reduce the error in both the seeding measurement and the thermodynamic equilibria estimation.

The other thermometric approach utilizes absorption spectrum of OH $X^2\Pi \rightarrow A^2\Sigma^+$ transitions, which is sensitive to temperature and pressure. The hydroxyl radical is highly reactive and short-lived, and is a common intermediate species in flames. The absorption spectra of OH have been widely studied to measure the OH concentration and temperature, mostly by line sources such as frequency scanning lasers [18, 19] and spectral lamp [20]. Recently, with the advance of light-emitting diodes (LED) in the ultraviolet (UV) spectral range, UV absorption spectra attracted more interest for combustion applications[21, 22]. In this work, a broadband deuterium lamp was used as the light source by which the OH absorption spectrum was measured, and the temperature was determined by simulating the measured spectra based on the HITRAN (high-resolution transmission molecular absorption database) database.

1.3 Thesis outline

The thesis is structured as follows: background knowledge encountered in this work is described in chapter 2, including general principles of atomic and molecular energy levels, discussion about spectroscopic properties, calculation of radiative transition intensities, and a brief illustration about temperature and the equilibrium state of reactions. In chapter 3, principles of the experimental methods are described. This covers the methods of TLAF, two-line alkali emission, and OH absorption spectroscopy, respectively. The main experimental equipment used in the work, including a multi-jet burner, external cavity diode lasers (ECDL), and a detector (camera),

are also described. The experimental results of the spectroscopic measurements are discussed in chapter 4. Chapter 5 presents a summary of the thesis work and an outlook for the future.

Chapter 2

Theoretical background

The purpose of this chapter is to present an overview of the background physics related to this study. The first section provides the basic principles of energy levels, and the second section introduces the intensity of radiative transitions including the line broadening mechanisms, which are necessary for both the spectral analysis and the simulation process, the calculation of the thermal emission intensity, and the simulation of molecular absorption spectrum. The kinetic considerations of the measured system are described in the third section of this chapter.

2.1 Energy levels

Spectroscopic techniques are based on the interaction between matter and electromagnetic radiation, in which knowledge about atomic and molecular energy levels is of great importance. Research concerning spectra and energy levels started since early 1800s when Fraunhofer firstly measured the spectral line wavelength with a spectrograph, and nowadays scientists are still studying the behavior of quantum particles and trying to provide fresh insights by some new approaches including quantum electrodynamics (QED) and quantum chromodynamics (QCD). The world of atom is fascinating and complicated. This section will only present some general concepts and relationships which are fundamental to the understanding of the thesis work, whereas Ref. [23, 24] are highly recommended for more ideas about atoms and molecules, respectively.

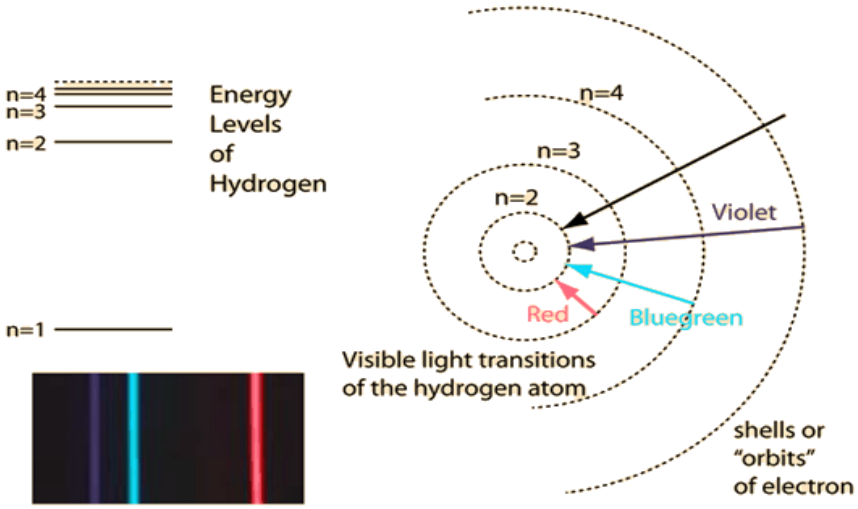

Fig. 2.1 The orbits of electron and the energy level of hydrogen. The emission spectrum of hydrogen atoms is shown in the bottom left, with transitions corresponding to the spectral lines to the right [25].

2.1.1 Atomic energy levels

Other than classical particles which can have arbitrary energies, the quantum mechanical particles, as bound by the electric field of the nucleus, can only take on certain discrete values of energy. These quantized discrete values of energy are called energy levels of the particle. Electrons in an atom are attracted to the protons in an atomic nucleus by electromagnetic force, and thus take on discrete energy values. The energy level of an atom depends not only on the configuration of its electrons but also on the couplings of different kinds interaction inside the atom. All information such as position, momentum, or internal energy of the atom is contained in its wave function, which is used to describe the wave-like nature of atoms. The wave function of an atom must satisfy the Schroedinger equation, which is complicated for non-hydrogen atoms with several electrons, and hence hydrogen atom is used to briefly illustrate the concept of energy level here.

As shown in figure 2.1, the energy levels of a Hydrogen atom are given by the famous Rydberg equation:

$$E = -\frac{E_0}{n^2} \tag{2.1}$$

where E_0 is the ionization energy and n is the principle quantum number. Energies are expressed as negative numbers because for a bounded electron it takes that much energy

to ionize from the nucleus. For a certain electron configuration, states that share the same energy values in the absence of electric or magnetic field are called degenerate energy states, and the number of different states is called the degree of degeneracy of the energy level, as denoted by a degeneracy factor g. Normally, the lowest energy level is called the ground level, and levels lying above the ground level are called excited levels. Electron volt (eV) is always used to express the energy difference between a ground and an excited energy level. Another physical quantity frequently used in atomic spectroscopy and also molecular spectroscopy is wavenumber ($\tilde{\nu}$), as defined by the number of wavelengths per unit length, and usually expressed in cm^{-1}. The internal energy E is of great importance in spectral line determination; since an electron has specific discrete energy values, it can transfer to a higher or lower energy level by absorbing or emitting a photon whose energy corresponds to the energy difference, and thus a large amount of information is available from different spectroscopic approaches.

2.1.2 Molecular energy levels

The energy levels of molecules are also quantized, but much more complex. The molecular energy structures are made up not only by the electronic energy levels but also by the vibrational and rotational energy levels. Molecules in the gas phase readily undergo rotation and translational motion [26]. Therefore, transitions among molecular energy levels, as caused by the dipole moment in the molecules, are much more complex. A simple sketch of the electronic, vibrational and rotational energy levels of hydrogen is shown in figure 2.2. The splitting between adjacent energy levels decreases in turn. In order of energy level spacing from largest to smallest, the spectral range where transitions can be observed corresponds to ultra-violet/visible, infrared, microwave, respectively [27].

Note that it is usually sophisticated for normal users to determine the molecular spectral parameters even in the case of elementary molecules. Alternatively, the spectroscopic parameters necessary for molecular transitions can be found from several spectral databases. HITRAN [29], as an acronym for high-resolution transmission molecular absorption database, is recognized as a comprehensive spectroscopic database and has been widely used in scientific research for the purposes of simulating and calculating of molecular spectra. The latest version, HITRAN2016 [29], provides the spectroscopic parameters of 49 species with more than 7 million spectral lines. The frequently used spectroscopic parameters include the line position, intensity, broadened half-width, Einstein A-coefficient, air-induced pressure shift, etc.

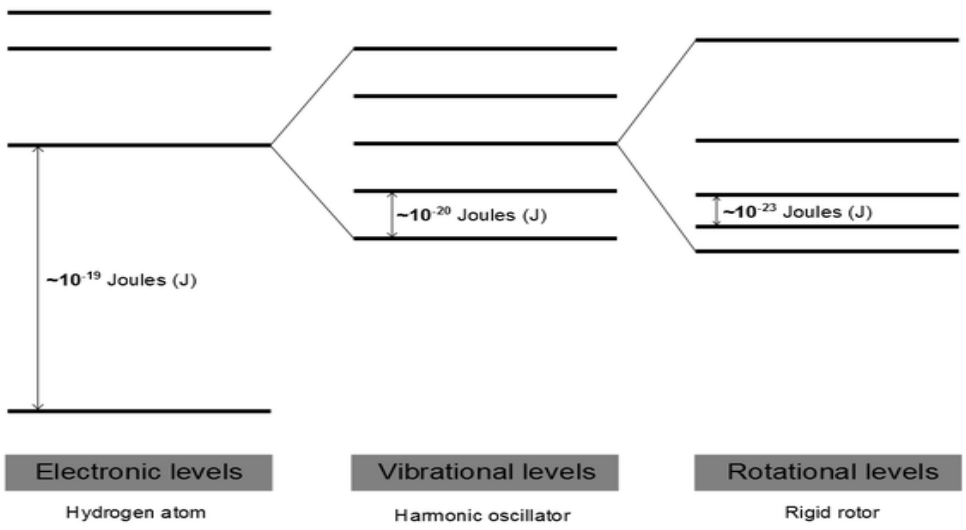

Fig. 2.2 Energy level separations in hydrogen. Electronic, vibrational, and rotational energy levels are shown with different energy splitting, which corresponds to $\sim$ 1 eV, $\sim$ 0.1 eV, and $\sim 10^{-4}$ eV, respectively [28].

2.2 Intensity of radiative transitions

This section provides principles of the intensities of radiative transitions related to the thermometric approaches. The mechanism of line broadening along with three shapes of line profiles are described in the first subsection. The intensity of thermal emission with self-absorption is described in the second subsection, and the principle of molecular absorption spectra is given in the third.

2.2.1 Line broadening

The photon energy emitted from a transition between certain energy levels in an atom or molecule is well-defined; nonetheless, the profile of measured spectral lines are always broadened and show finite width. Normally, the spectral line appearing to be broadened is caused by the resolution of the spectral apparatus. But even if the apparatus has a fairly high spectral resolution, the broadening will still exist due to the spectral distribution of the photons being absorbed or emitted by the atomic or molecular samples.

Particles that stay at excited states have a finite lifetime, and according to the uncertainty principle, this will lead to a spectral broadening due to the uncertainty in energy. This intrinsic broadening is called the natural broadening. It is insignificant compared to the broadening caused by collisions or the Doppler effect. For this reason, the natural line width will not

be discussed within this thesis. The other two most common broadening mechanisms are discussed separately in this part, and a combined line shape known as the Voigt profile is also described.

Doppler broadening

The thermal motion of atoms or molecules introduces the Doppler broadening to the spectral profile, i.e., the frequency of the radiation emitted or absorbed by an atom or molecule appears to be broadened due to the thermal motion. If the particle moves toward a stationary detector, the readout frequency will become higher, and vice versa. The velocity distribution at a certain temperature is given by the Maxwell - Boltzmann distribution:

$$f(v) = \left(\frac{m}{2\pi k_B T}\right)^{3/2} 4\pi v^2 \exp(-\frac{mv^2}{2k_B T}) \tag{2.2}$$

where v is the speed of the particle, m is the mass, T is the thermodynamic temperature, and k_B is the Boltzmann constant, which equals to $1.38 \times 10^{-23} J \cdot K^{-1}$. By considering the Doppler frequency shift of all involved species and averaging over the velocity distribution, the Doppler broadening can be described by the Gaussian function as in equation 2.3.

$$g_D(\nu) = \frac{c}{\nu_0}\sqrt{\frac{m}{2\pi k_B T}} \exp[-\ln 2\,(\frac{\nu - \nu_0}{\gamma_D})^2] \tag{2.3}$$

Here $g_D(\nu)$ is the Doppler line shape function normalized as $\int_{-\infty}^{\infty} g(\nu)d\nu = 1$, ν_0 is the transition center frequency, and c is the speed of light. The half width at half maximum (HWHM) induced by the Doppler effect is denoted by γ_D, which is given by

$$\gamma_D = \frac{\nu_0}{c}\sqrt{\frac{2\ln 2\; k_B T}{m}} \tag{2.4}$$

It should be emphasized here that the Doppler broadening is only temperature dependent. For the transitions of OH at $0.3\,\mu\mathrm{m}$, the Doppler line width is 0.251 cm^{-1} at 2000 K and 0.097 cm^{-1} at 300 K.

Collision broadening

Collision broadening is also known as pressure broadening, which is resulted from the perturbations of colliding molecules and atoms. Collision broadening can be described by a Lorentzian

profile, namely

$$g_c(\nu) = \frac{1}{\pi} \frac{\gamma_c}{(\nu - \nu_0)^2 + (\gamma_c)^2} \tag{2.5}$$

where γ_c is the collision-induced HWHM depending on the pressure, temperature, local gas composition and number density. The collision line width at low pressure is usually negligible comparing to the Doppler broadening. Nonetheless, it is considerable for atmospheric or high-pressure transitions. Within the scope of this thesis, for particles at 1 atm and elevated temperature (1500 $\sim$ 2000 K), these two broadenings are comparable, and thus a so-called Voigt line shape is introduced as a combination of both broadening mechanisms, which will be discussed in the next subsection.

Voigt profile

Under the condition where both Doppler and collision effects are considered, an overall broadening can be calculated from the convolution of these two spectral line shapes. The combination is described by a so-called Voigt line shape function, which provides the most accurate line shape in a flame environment, as given by

$$g(\nu) = \frac{2}{\gamma_D} \frac{a}{\pi} \sqrt{\frac{\ln 2}{\pi}} \int_{-\infty}^{\infty} \frac{\exp(-y^2)}{a^2 + (x - y)^2} dy \tag{2.6}$$

where a and x are defined as:

$$a = \sqrt{\ln 2} \frac{\gamma_c}{\gamma_D} \tag{2.7}$$

$$x = \sqrt{\ln 2} \frac{(\nu - \nu_0)}{\gamma_D} \tag{2.8}$$

The Voigt parameter a demonstrates the relative weight of the Doppler and collision broadening contribution. For 0 < a < 1, the line shape is Doppler dominated, while for a > 2 , the broadening becomes collision dominated [30]. A comparison of the three spectral profiles is shown in figure 2.3. Note that when the Voigt profile becomes Lorentzian predominant, broad wings of a large frequency extent show up, which is absent in the Gaussian profile.

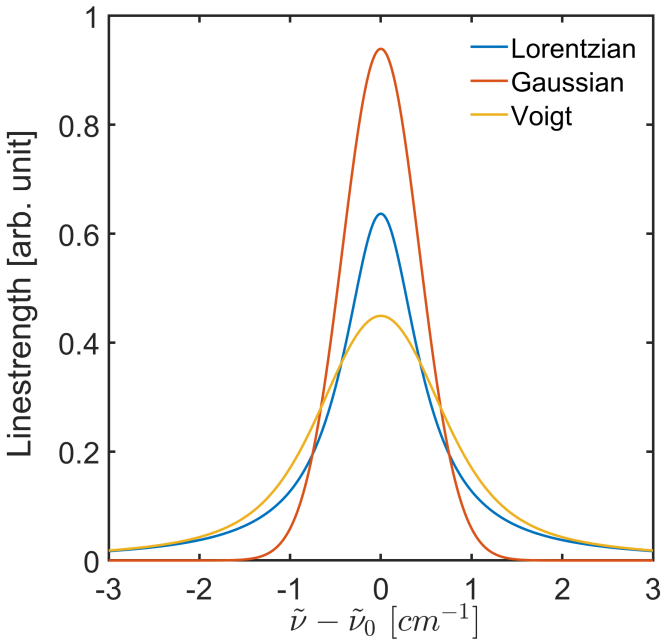

Fig. 2.3 Comparison of Lorentzian (collision-), Gaussian (Doppler-) and Voigt broadened line shapes. It should be mentioned that the HWHM of the Lorentzian profile is identical to the Gaussian profile, nevertheless, the line-center strength of the formal is nearly 30 percent lower than the latter. The Voigt profile is a combination of both broadening contributions, which equals to the convolution of the two profiles.

2.2.2 Intensity of thermal emission lines

An atom in an excited state will spontaneously jump to a lower energy state in the form of photon emission as aforementioned in section 2.1.1. When the atomic concentration is low, all photons generated inside the hot gas will be collected, and the outgoing radiance B of a certain emission line is expressed by equation 2.9 [31].

$$B = \frac{A_{qp} hc}{4\pi\lambda_0} \int_0^l n_q(l')dl' \tag{2.9}$$

Here l is the thickness of the gaseous light source, $hc/\lambda_0$is the emitted photon energy. The upper and the lower energy states are denoted by q and p, respectively. The number density of the excited state along the line of observation is described by $n_q(l')$, and A_{qp} is the Einstein coefficient of spontaneous emission.

Assume the atoms distribute homogeneously over the observation volume, and replace the number density of the excited state n_q by the number density of atoms n_a according to the Boltzmann distribution law (see equation 2.17 in section 2.3). Then the equation 2.9 is reduced to

$$B = \frac{hc}{4\pi\lambda_0}\frac{g_q}{Q}\exp(-\frac{E_q}{kT})\,A_{qp}n_a l \tag{2.10}$$

where E_q is the energy of the upper state, g_q is the degeneracy, and Q is the partition function. For transitions involving ground levels, E_q is usually significant larger than kT under flame conditions. Therefore, equation 2.10 shows that for given n_a and l, the radiance is strongly dependent on the temperature, making it possible to determine temperature from atomic emissions.

The emission intensity ratios between atomic Na and K were measured in this work, which according to equation 2.10 can be expressed by:

$$\frac{B_1}{B_2} = \frac{A_{qp,1}}{A_{qp,2}}\frac{g_{q,1}}{g_{q,2}}\frac{\lambda_{0,2}}{\lambda_{0,1}}\frac{n_{a,1}}{n_{a,2}}\exp(\frac{E_{q,2}-E_{q,1}}{kT}) \tag{2.11}$$

where the parameters concerning Na and K are denoted by the subscript 1 and 2, respectively.

For the case of high atomic concentration, the effect of self-absorption has to be considered. That is, photons emitted inside the atomic light source may be re-absorbed by atoms of the same element lying in the ground state, and thus the radiance intensity of the outgoing light may be reduced. According to the Beer-Lambert law, the attenuation of light is dependent on the optical path l, the atomic density n_a (for the case of a transition from the ground state,

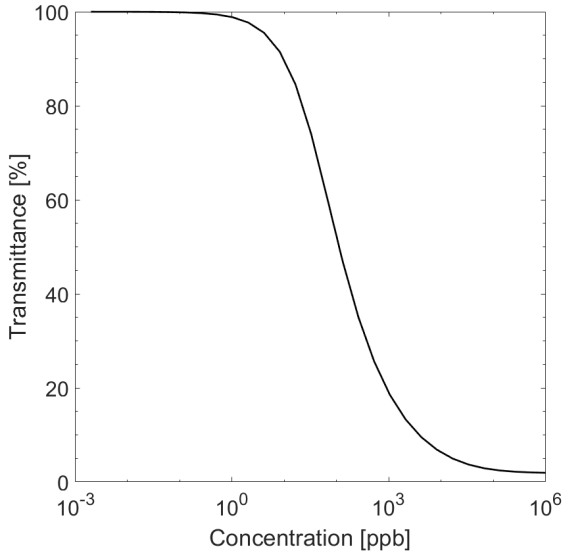

Fig. 2.4 Calculated transmittance of the potassium spontaneous emission due to the self-absorption. Note that the atomic concentration is shown in a logarithmic coordinate. The effect of self-absorption was simulated with a temperature of 2000 K and an optical path of 5 cm.

otherwise n_p), and the atomic absorptivity $\kappa(\nu)$ [32], as expressed by

$$I_t = I_0 \, \exp[-\kappa(\nu) \, n_a \, l \,] \, . \tag{2.12}$$

Here I_0 is the incident intensity and I_t is the transmitted intensity. The atomic absorptivity can be calculated from[31]

$$\kappa(\nu) = 3.975 \times 10^{-2} \, g(\nu) {\lambda_0}^2 A_{qp} \frac{g_q}{g_p} \tag{2.13}$$

where $g(\nu)$ is the normalized line shape described by the Voigt profile. The radiance of thermal emission with self-absorption can thus be calculated by:

$$B_t = \frac{\int_{l'=0}^{l} \int_{\nu=0}^{\infty} g(\nu) \exp[-\kappa(\nu) \, n_a \, l \,] d\nu dl'}{\int_{l'=0}^{l} \int_{\nu=0}^{\infty} g(\nu) \, d\nu dl'} \cdot B \tag{2.14}$$

Here B is the outgoing radiance without self-absorption.

Figure 2.4 shows the transmittance of the potassium spontaneous emission as a function of atomic potassium concentration at 2000 K and 5 cm absorption length. It can be seen that all emitted light gets transmitted when the atomic K contraction is lower than 1 ppb, and the fraction of transmitted light decreases rapidly with the increase of concentration. When the atomic K concentration approaches the ppm level, more than half of the emitted light is reabsorbed in the observation volume, and the transmitted light is mainly determined by the effect of self-absorption.

2.2.3 Simulation of molecular absorption spectrum

A model of OH absorption spectrum was established for the temperature determination where the necessary molecular constants were taken from the HITRAN database. The absorption line intensity parameter S_i at experimental temperature can be calculated by

$$S_i = S_i(T_{ref}) \cdot \frac{Q(T_{ref})}{Q(T)} \cdot \frac{\exp(-c_2 E_i / T)}{\exp(-c_2 E_i / T_{ref})} \cdot \frac{[1 - \exp(-c_2 \nu'_{0,i} / T)]}{[1 - \exp(-c_2 \nu'_{0,i} / T_{ref})]}. \tag{2.15}$$

Here $S_i(T_{ref})$ is the line intensity at a reference temperature (296K), E_i is the lower state energy in the unit of cm^{-1}, c_2 [cm·K] is the second radiation constant, $\nu'_{0,i}$ is the transition wavenumber for line i with pressure-induced line shift, and $Q(T)$ is the partition function. At a

given temperature T, all parameters involved in equation 2.15 are extracted from the HITRAN database, and the overall transmitted spectrum can be estimated by

$$I_t = I_0 \exp[-n\, l\, S_i\, g(\nu)] \tag{2.16}$$

where n is the molecular number density of absorbing species, l the path length, and $g(\nu)$ is the normalized Voigt line shape function. The optical depth $\tau = -\ln \frac{I_t}{I_0}$ is always used to describe absorption profiles. Figure 2.5 shows a comparison of OH absorption spectra near 32300 cm^{-1} at different temperatures. Obviously, the OH radical possesses more absorption lines at 1500 K than 300 K, and the spectral line intensities are also temperature dependent. Therefore, it is feasible to obtain temperature from molecular spectroscopy.

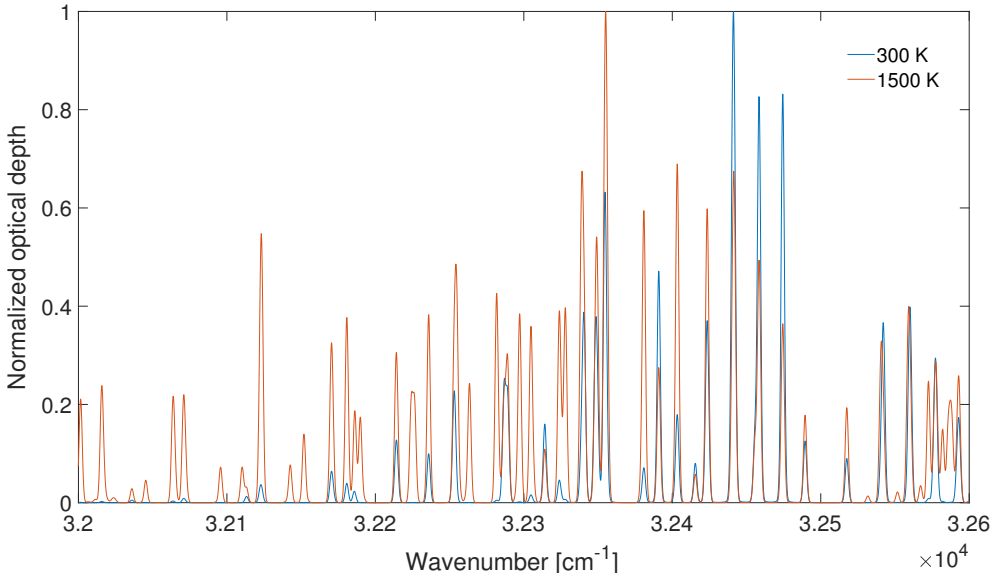

Fig. 2.5 Simulated spectra of the the OH (A(0) - X(0)) band at 300 K and 1500 K. An additional Gaussian instrumental broadening was added in the simulation with a line width of 2.5 cm^{-1}. The optical depths were normalized to the same intensities of both spectra to emphasize the structure variation of the OH band at different temperatures.

2.3 The equilibrium state

When a metal vapor is seeded in tracer level into a flame environment, the flame and the hot gas mixtures can be treated approximately as a heat bath with constant temperature. In this circumstance, the system will spontaneously reach a state of thermodynamic equilibrium. The equilibrium state implies detailed balance, which means that the reaction rate of every

activation process and its reverse deactivation process should be balanced [31]. Under the condition of thermodynamic equilibrium, dynamic properties of the system, including the overall reaction rates, the energy distribution, and the spectral characteristics, are all governed by the temperature. Temperature is a universal parameter of the system; the equilibrium distribution is dependent on the total element concentration, component properties, and the temperature, avoiding the detailed knowledge about the individual species concentration and the distribution functions over the various degrees of freedom.

The velocity distribution of a state in equilibrium is given by the Maxwell law, as mentioned in section 2.2.1. The population of different energy levels of a certain species is described by the Boltzmann distribution law, given by [32]

$$\frac{N_j}{N} = \frac{g_j}{Q} \exp(\frac{-E_j}{k_B T}) \tag{2.17}$$

where N_j stands for the number density of the species in the energy level E_j with respect to the ground level ($j = 0$), N is the total number density, g_j is the degeneracy of the level, k_B and T have their usual meanings. The partition function Q for certain particles is only temperature dependent, as defined by

$$Q \equiv \sum_{i=0}^{\infty} g_i \exp(\frac{-E_i}{k_B T}) \tag{2.18}$$

Here the summation contains all the possible energy levels, along with the ground level. When the temperature satisfies that $k_B T$ (0.17 eV at 2000 K) is relative small comparing to the lowest excited level, the value of Q can be satisfactorily approximated to the first term g_0.

Under actual flame conditions, the system is not strict adiabatic due to the interaction between flame gases and surroundings, nonetheless, these interactions occur in a comparative slow scale with respect to the energy transfers in the hot gas environment. Therefore, a state of local thermodynamic equilibrium is established, leading to a concept of local temperature which is still essential for flame relevant studies.

Chapter 3

Methods

This chapter describes the main equipment as well as the experimental and analysis methods. The first section describes the characteristics and parameters of the burner, the lasers, and the camera used in this work. The experimental considerations of the TLAF thermometry, the two-line alkali emission method and the OH UV absorption spectroscopy are presented in the following sections, respectively. The spectral fitting methods of the OH absorption spectrum are also described in the last section.

3.1 Experimental equipment

3.1.1 Multi-jet burner

The use of a satisfying burner is of great importance for combustion related experiments. The burner should be able to provide a variety of controllable and reproducible combustion environments for the need of different experimental purposes. A novel multi-jet burner [10], as shown in figure 3.1, was used for all measurements involved in this thesis. The burner could provide flames with homogeneous temperature distribution in many variable conditions. The burner consisted of a jet-flow chamber and a co-flow chamber, with 181 jet tubes evenly distributed in a large rectangular outlet. Each jet has a length of 183 mm to develop the laminar flow and is surrounded by six small holes, which are connected to the co-flow chamber. At the top of the jet, a shielding ring with a height of 18 mm was added to the burner. In this way, laminar flames could be well established on the jet with homogeneous co-flow gases mixed around, and the burnt gas was separated from the ambient air. Additionally, the inside of the shielding ring was encompassed by four asbestos plates, which had a thickness of 3 mm for

preventing the heat loss from the burner surface. The size of the rectangular burner outlet is 100 mm × 60 mm. This comparable broad outlet offered sufficient optical area for various laser-based combustion measurements. Normally, an iron stabilizer with the same size as the rectangular outlet was placed 35 mm above the top of the burner to further stabilize the flame.

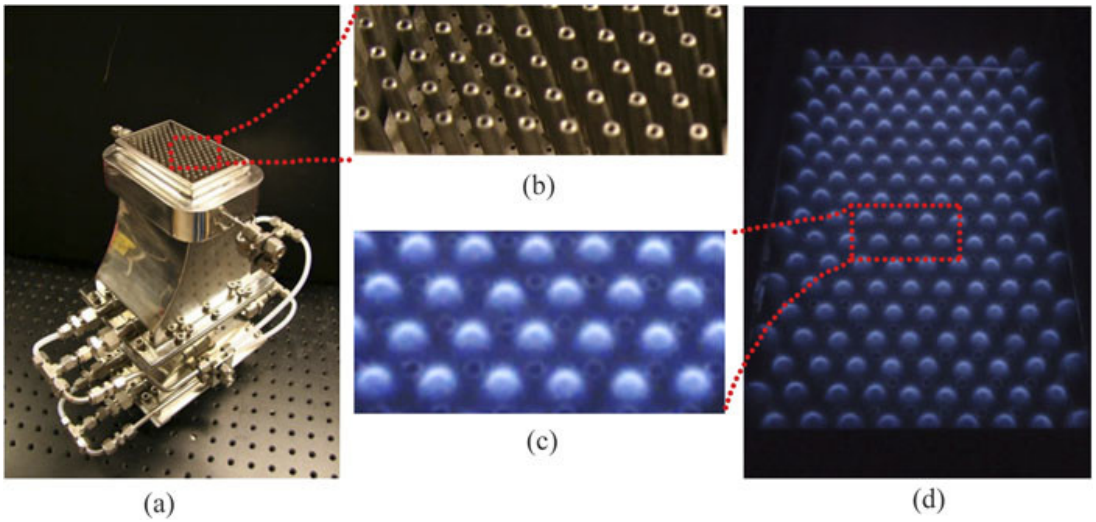

Fig. 3.1 Photos of the multi-jet burner reprinted from [10]. (a): An oblique view of the burner. (b): A detailed view of the burner outlet. (c) and (d): Typical premixed flames generated on the burner.

The adjustment of different flow rates was controlled by several mass flow controllers (Bronkhorst High-Tech) with an accuracy of ± 0.8%. Although all experimental environments involved in this thesis were based on laminar premixed flames, both premixed and diffusion flames can be readily generated on the burner by adjusting the gas composition of the jet-flow and the co-flow, with temperatures ranging from 1000 K to 2000 K. In addition, the burner design also allows for seeding of different tracer species into the flame in the form of tiny liquid droplets or gases. The seeding additives carried by the carrier gas (N_2 in most conditions) can be seeded from the jet-flow or the co-flow and distribute homogeneously in the hot gas mixture.

3.1.2 External cavity diode laser

Three external cavity diode lasers (ECDLs) were employed in this work, centering at 410 nm, 451 nm, and 769 nm, respectively. Littman and Littrow configurations of ECDLs are the two most common configurations. Both of them use a diffraction grating to selectively reflect some part of emission light back into the laser and the feedback of the reflected light forces the laser into single-mode operation. In a Littman configuration, a mirror is used to reflect the

first-order diffracted light back to the grating then being fed back into the laser. The ECDLs used in this work are Littrow designs, where the first order diffracted beam is directly reflected back to the laser diode, and the output wavelength is adjusted by changing the grating angle. Because of the existence of both internal and external feedback, the output wavelength is not always continuous. The unstable status where the wavelength jumps discontinuously is called mode hops. During the process of measurement, the stability of the laser was monitored by a Fabry-Perot interferometer to assure single-mode operations. Toptica DL100pro and DL100 ECDLs were adopted in this work, which have narrow line widths (< 1MHz), high temperature-change stability, and large mode-hop-free tuning range (up to 30 GHz at 769 nm).

3.1.3 Camera

A PI-MAX 3 model 1024i camera from Princeton Instruments was employed in this work to capture the fluorescence and emission signals. It is an intensified charge-coupled device (ICCD) camera with good signal-to-noise ratio, excellent sensitivity, and high gate speed. The spectral coverage of the camera is wide enough for all wavelengths involved in this work from ultraviolet to near-infrared, especially for potassium lines at 766 nm and 769 nm where most cameras are not able to detect. During the TLAF measurement, the camera was equipped with a 451 nm filter and synchronized with an optical chopper to record the laser-induced fluorescence signals from indium atoms. In the alkali emission measurement, a stereoscope with two filters was mounted in the front of the camera to capture the emission light from sodium atoms and potassium atoms at the same time.

3.2 Two-line atomic fluorescence thermometry

In this section, the general principles and the experimental methods of the TLAF technique are described. The first part of this section describes the detection scheme used in the work. A brief derivation of the temperature expression is given in the second part. The third part illustrates the experimental setup and the measuring procedures.

3.2.1 Detection scheme of TLAF

The TLAF technique is based on a laser-induced fluorescence (LIF) method, and this technique was used in the present work to determine gas temperature at different flame conditions.

As shown in figure 3.2, the two lower electronic levels of an atom are successively excited to a common upper level, and the temperature can be deduced from the ratio of the two laser-induced fluorescence signals.

Table 3.1 Spectroscopic properties of indium atom involved in TLAF. Data retrieved from [33]

	Wavelength (nm)	Transitions	Energy levels (cm^{-1})	Einstein A cofficient (10^8 s^{-1})
Indium	410	$5p_{1/2}$ - $6s_{1/2}$	0 - 24372.96	0.50
	451	$5p_{3/2}$ - $6s_{1/2}$	2212.60 - 24372.96	0.89

TLAF temperature measurement using indium atom similar to the one described in [13] was performed in this work. The relevant physical constants of indium are shown in table 3.1. For indium atom, the energy levels 1, 2, and 3 represent for the $5p_{1/2}$, $5p_{3/2}$, and $6s_{1/2}$ levels, respectively, and the transition $1 \rightarrow 3$ pumped at λ_{31} corresponds to 410 nm while λ_{32} corresponds to 451 nm. Although only two lower levels and one upper level are shown in the figure, it should be mentioned that these three levels all have hyperfine structures. The $5p_{1/2}$ and the $6s_{1/2}$ levels are both split into two hyperfine levels, while the $5p_{3/2}$ level is split into four hyperfine levels. The relative transition intensities between the hyperfine levels can be calculated from the Clebsch-Gordan coefficients [34], and thus the spectral profile of the transitions $5p_{1/2} \rightarrow 6s_{1/2}$ and $5p_{3/2} \rightarrow 6s_{1/2}$ is well-defined. It should be noted that when an atom with two different lower energy levels is excited to an upper state, it will de-excite in the form of fluorescence to either level 1 or level 2, but only fluorescence signals with frequency corresponding to the energy difference between level 3 and 2 were detected in the present work as shown in figure 3.2. This detection scheme was preferred for the following reasons. Firstly, fluorescence signals collected have the same wavelength, and thus only one detector is needed, which significantly simplifies the experimental setup and also avoid the need for a calibration measurement. Secondly, compared with the transition between level 3 and 1, the de-excitation to the level 2 has a higher transition probability. Thirdly, the signal interference from other common species (C_2, CH, etc.)in the flame can be largely reduced at 451 nm [12].

3.2.2 Temperature derivation

The indium atoms in the flame environment exhibit several excitation and de-excitation processes. Taking all of them into consideration, the atomic population of a particular energy state can be deduced when thermal equilibrium is assumed, as shown in equation 3.1 [6]:

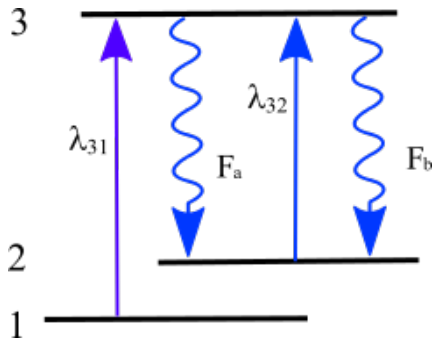

Fig. 3.2 The scheme of the adopted TLAF measurement where level 1 and 2 are two lower electronic levels and level 3 is the upper level. F_a and F_b denote the subsequent fluorescence signals induced by the incident laser with wavelength of λ_{31} and λ_{32} respectively .

$$N_i \cdot \frac{I_{i3}B_{i3}}{c} = N_3 \cdot (A_{31} + A_{32} + Q_3 + \frac{I_{i3}B_{3i}}{c}) \tag{3.1}$$

Here, N_i is atomic population of the state i, in which the subscript is consistent with the one used in figure 3.2, . I_{i3} is the irradiance of the laser which excite the atom from the state i to the upper state 3, and c is the velocity of light. B_{i3}, B_{3i} and A_{3i} are the Einstein coefficients of stimulated absorption, stimulated emission and spontaneous emission respectively. Q_3 is the quenching rate which stands for the de-excitation via non-radiative processes.

The stimulated emission from the upper state is negligible owing to the low population, and this gives:

$$N_3 = c \cdot (\frac{N_i I_{i3} B_{i3}}{A_{31} + A_{32} + Q_3}), \tag{3.2}$$

where the Einstein coefficients are related to the wavelength of the light (λ) and the degeneracies (g) of each level [35] :

$$\frac{A_{31}B_{23}}{A_{32}B_{13}} = \frac{g_1}{g_2}(\frac{\lambda_{13}}{\lambda_{23}})^3 \tag{3.3}$$

At low seeding concentration, the attenuation of the laser power and the self-absorption of the emitted fluorescence are negligible, and thus the fluorescence intensity from the transition $3 \rightarrow i$ detected by TLAF is expressed as [36]:

$$F_{3i} = A_{2i} N_3 V \frac{hc\Omega}{4\pi\lambda_{3i}} \tag{3.4}$$

Here F_{3i} is the intensity of the laser-induced florescence, h is the Planck constant, V is the probe volume, and Ω is the solid collection angle. As earlier mentioned, for conditions of

thermal equilibrium, the populations of the states are dependent on the temperature through the Boltzmann distribution.

$$\frac{N_1}{N_2} = \frac{g_1}{g_2} \exp(-\frac{\Delta E}{k_B T}) \tag{3.5}$$

Equation 3.5 in conjunction with equation 3.2, 3.3 and 3.4 gives the final TLAF expression for temperature. The resulting equation for aforementioned detection scheme is given as:

$$T = \frac{\Delta E / k_B}{\ln(\frac{F_a / I_{13}}{F_b / I_{23}}) + 3\ln(\frac{\lambda_{23}}{\lambda_{13}}) + \ln(\frac{A_{32}}{A_{31}})} \tag{3.6}$$

where ΔE is the energy difference between level 1 and level 2 , and F_a, F_b are usually preferred to denote the fluorescence excited from the lower ground and the upper ground level, respectively, as shown in figure 3.2.

3.2.3 Experimental method

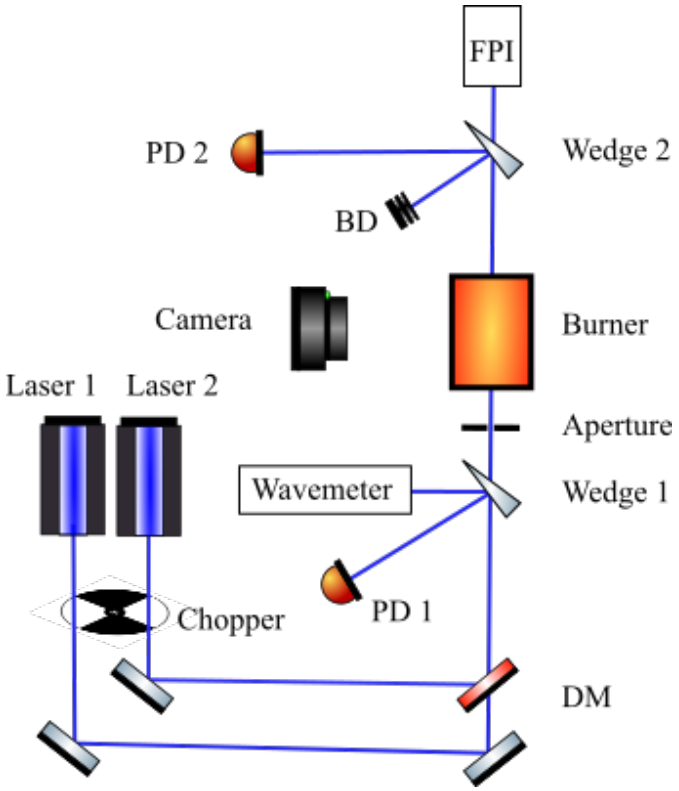

Fig. 3.3 Schematic diagram of the TLAF setup. DM: dichroic mirror, PD: photodiode, BD: beam dump, FPI: Fabry-Perot interferometer.

The optical setup of the TLAF measurement is presented in figure 3.3. Two external cavity diode lasers (Toptica DL 100 and DL 100 PRO) with wavelengths centered at 451 nm and 410 nm, respectively, were used to sequentially excite the indium atoms. The spectral line widths of both lasers are narrower than 1 MHz, which makes it possible to characterize the atomic absorption profile needed in the temperature derivation. In front of the laser outlet, an optical chopper (Thorlab MC1000A) was mounted to block and open the laser beams. To simplify the detecting procedure, the chopper was aligned with a short period during which both lasers were blocked, to allow the spectral background being captured almost simultaneously. Mirrors include a dichroic mirror were used to overlap the lasers. Before guiding into the burner, the light was split by a wedged glass plate to monitor the laser wavelength by a wavemeter (High Finesse UV 6-200) as well as record the reference laser power by a reference photodiode (Thorlab PDA 1000A, PD 1 in figure 3.3). The wavelength meter has a resolution of 0.1 pm, and it was corrected by the scanned absorption profiles of indium atom at both 410 nm and 451 nm (see figure 3.4). After each measurement, the photodiode was calibrated by a thermopile-based power meter (Thorlab S302C). An intensified CCD camera (Princeton Instrument MAX 3 1024i) equipped with a 451 nm filter was used to record the laser-induced fluorescence only from the upper ground state as previously mentioned. After the interrogation region, a second wedged glass plate was mounted. One beam of the reflected light was sent to another photodiode (Thorlab PDA 1000A, PD 2 in figure 3.3) to monitor the degree of atomic absorption, while another part of the light was sent to a scanning Fabry-Perot interferometer (Toptica FPI100) to make sure the single-mode operation of the lasers.

The indium can be seeded into the flame in the form of trichloroindium ($InCl_3$) or trimethylindium (TMI). The $InCl_3$water solution was introduced to the premixed gas mixture by an ultrasonic fog generator, while the TMI was carried by a specially designed bubbler system [37] which can provide a stable seeding concentration. The bubbler system was submerged in an antifreeze bath with a temperature of 10 °C, and the TMI vapor was carried to the burner by high purity (99.9%) nitrogen carrier gas. The seeding concentration can be easily adjusted by either alter the bath temperature or change the flow speed of the carrier gases. For the temperature measurement, the quantity of indium atom needed in the hot gas region is very small, with a concentration of less than 1 ppm.

During the measurement, the rotary chopper was running at a frequency of 3 Hz, and it was synchronized with the camera so that three images were recorded each period, as

aforementioned: the fluorescence induced by the 451 nm laser, the fluorescence induced by the 410 nm laser, and the background. The exposure time for each image was 10 ms. Before the temperature measurement, the absorption profiles at both 410 and 451 nm were measured by excitation scans, i.e., changing the laser wavelength and recording the induced fluorescence simultaneously. The results are shown in figure 3.4. For the temperature measurements, the wavelengths of lasers were fixed at the peaks of the absorption profiles.

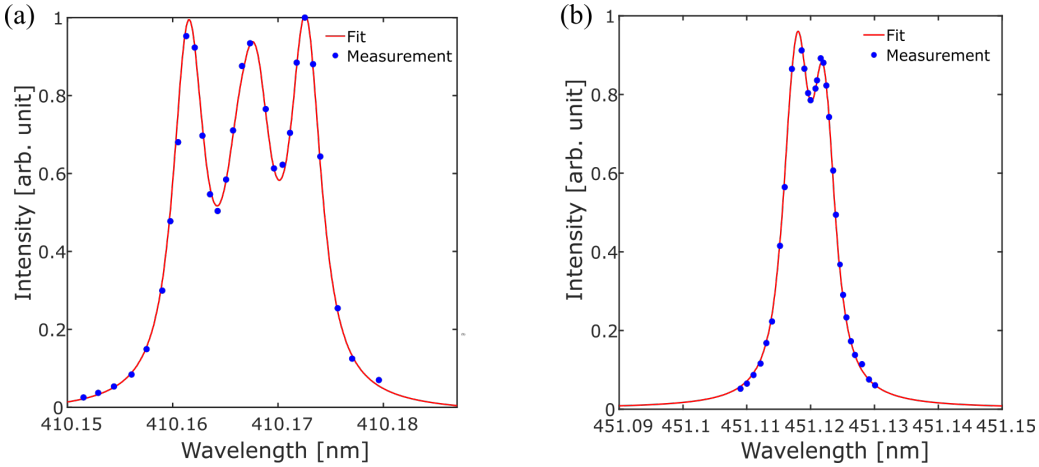

Fig. 3.4 Excitation scans of the indium absorption line shape. (a): $5p_{1/2} \rightarrow 6s_{1/2}$, (b): $5p_{3/2} \rightarrow 6s_{1/2}$. The scanning was conducted in a CH_4/ O_2/ N_2/ air flame with an oxygen content of 1% and a corresponding temperature of 1850 K, and the laser beams were 5 mm above the burner outlet.

3.3 Alkali emission spectroscopy

In this work, the relative intensities of two thermal emission lines of both the same element and two different elements were used to evaluate temperature. Sodium and potassium were adopted as seeding elements for their relatively simple atomic structure with only one valence electron and colorful light emitted in flame. The spectroscopic properties of these two elements are shown in table 3.2. The ratios between the spectral lines of Na at 589 nm and the K lines at 766 nm were measured as well as the ratios between K lines at 404 nm and 766 nm for the purpose of temperature determination.

The description of alkali thermal emission is presented in section 2.2.2, and the experimental method of the two-line method (in emission) will be described in this section.

As shown in figure 3.5, the experimental setup of the two-line emission measurement is similar to the TLAF setup. The difference is, in the TLAF measurement, the camera worked

Table 3.2 Spectroscopic properties of alkali metal fluorescence involved in this work.

	Wavelength [nm]	Einstein A coefficient [10^7 1/s]	Energy levels $\bar{\upsilon}_q - \bar{\upsilon}_p$ [cm^{-1}]	Degeneracy $g_q - g_p$	Transition [Notation nl_j]
Na	589.00	6.160	16973.37 – 0	4 – 2	$3p_{3/2} - 3s_{1/2}$
	589.59	6.140	16956.17 – 0	2 – 2	$3p_{1/2} - 3s_{1/2}$
K	404.41	0.116	24720.14 – 0	4 – 2	$5p_{3/2} - 4s_{1/2}$
	404.72	0.107	24701.38 – 0	2 – 2	$5p_{1/2} - 4s_{1/2}$
	766.49	3.790	13042.88 – 0	4 – 2	$4p_{3/2} - 4s_{1/2}$
	769.90	3.740	12985.17 – 0	2 – 2	$4p_{1/2} - 4s_{1/2}$

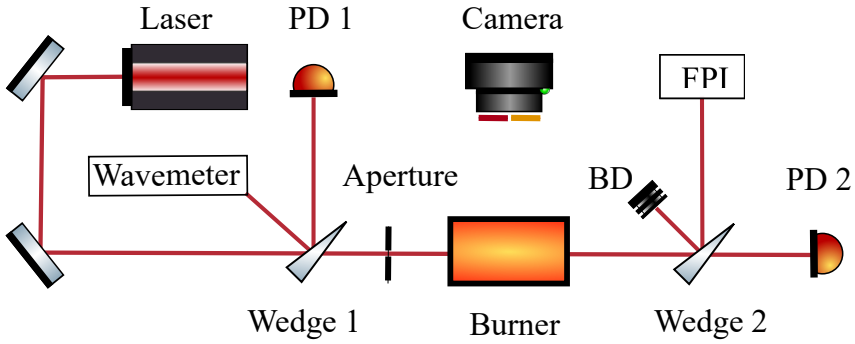

Fig. 3.5 Schematic diagram of the experimental setup. DM: dichroic mirror, PD: photodiode, BD: beam dump, FPI: Fabry-Perot interferometer.

synchronously with the lasers to capture the LIF signal. While in the emission measurement, the camera and the laser worked separately. The ICCD camera (Princeton Instrument MAX 3 1024i), mounted with a stereoscope and two filters, was used to simultaneously record the spontaneous radiation from the burnt gas at two wavelength ranges. For the measurement of Na/K intensity ratios, the filters employed were a 589 nm bandpass filter and a 766 nm bandpass filter, while for the measurement of K 404 nm and 766 nm lines, another 404 nm filter was used. The bandpass filters involved in this experiment each has a HWHM of $\sim$ 5 nm. In the latter measurement, an OD 9 filter was settled in front of the 766 nm bandpass filter due to the very intense emission lines at 766 nm compared with the 404 nm ones. The tunable diode laser system (Toptica DL 100), centering at 769.9 nm, was employed for the concentration measurement of atomic potassium by tunable diode laser absorption spectroscopy (TDLAS) method. The laser signals before going through the burner were monitored by a photodiode and a wavemeter; after the burner, a second photodiode was placed to record the absorbed waveform and calculate the concentration of atomic potassium. The single-mode operation and the scanning range of the laser were monitored by a Fabry-Perot interferometer, which in this case was approximately 30 GHz. More information about the TDLAS method can be found

in [38, 39]. For each flame condition, the concentration of atomic potassium was measured firstly, and then the thermal emission was recorded with the laser blocked.

A water solution of Na_2CO_3 (0.05 mol/L) and K_2CO_3 (0.05 mol/L) was used to produce atomic Na and K. The alkali solution was gasified by an ultrasonic fog generator and introduced to the premixed gas mixture in the form of fog. The fog of alkali water solution was atomized after passing through the flame front, and the chemical equilibrium state was fully established at the measurement position, which is about 5 mm above the burner outlet.

At first, the experimental setup was designed with three separate spectroscopic subsystems: the capture of thermal emission, K concentration measurement by TDLAS method, and the absorption measurement of both Na and K. The burner was settled on a slide rail and moved to different positions for the purpose of different measurements. In the third part, a radiant heat lamp was adopted as the light source to measure the ratio of the number density between atomic K and Na to further determine the absolute sodium concentration, and the incident light was reflected ten times in the interrogation volume to increase the optical path length for improved the absorption profile. However, the absorption profiles were still not well-recognized due to the low atomic concentration and poor signal-to-noise ratio. Therefore, final knowledge about Na concentration was not experimentally obtained, but simulated by the software CHEMKIN-PRO [40] according to the K concentration.

3.4 Hydroxyl absorption spectroscopy

In this section, the feasibility of thermometry using OH absorption spectrum was studied. The ultraviolet (UV) absorption spectra of hydroxyl (OH) molecule were acquired, and the experimental spectra were simulated by spectral fitting methods to extract the temperature information. The experimental setup is described, and the spectral fitting methods are explained in this section.

3.4.1 Experimental method

The optical setup of the UV absorption measurement is shown in figure 3.6. A deuterium lamp was adopted as the broadband UV light source, which was collimated to a light beam of about 10 mm by an aperture and a parabolic mirror. The incident light was reflected six times in the interrogation volume by UV enhanced aluminum mirrors to increase the optical path

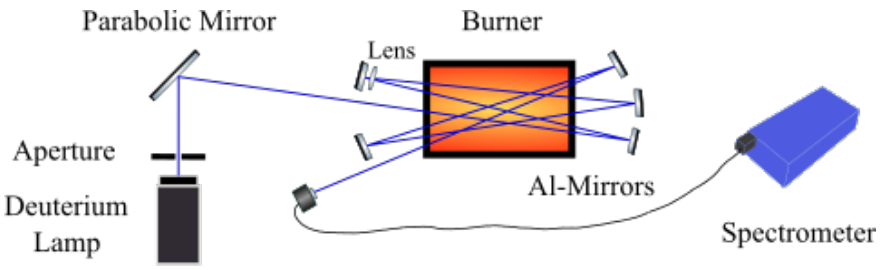

Fig. 3.6 Schematic diagram of the UV absorption spectroscopy setup.

length to further improve the absorption profile. A spherical lens (f=1000+) was mounted to collimate the light beam. After the burner, the transmitted light was collected by a spectrometer (Shamrock 750, Andor). The UV light was aligned $\sim$ 2 mm above the burner, where the hot flue gas was provided in a premixed flame with a global equivalence ratio of 0.6. The flow rates of the studied flame are shown in table 3.3.

Table 3.3 Flow rates (298 K and 1 atm) of the studied flame case for the UV absorption measurement.

Jet-flow (L/min)			Co-flow (L/min)	O_2 in burnt gas (%)
CH_4	O_2	N_2	N_2	
1.56	5.21	13.46	9.90	6.9

3.4.2 Spectral fitting method

The simulation methods of the OH absorption spectrum based on HITRAN database has been discussed in section 2.2.3. In this work, a MATLAB code was developed to evaluate temperature by simulating the measured OH spectrum using a least-square algorithm. A flow chart showing the optimization algorithm of the spectral fitting process is shown in figure 3.7.

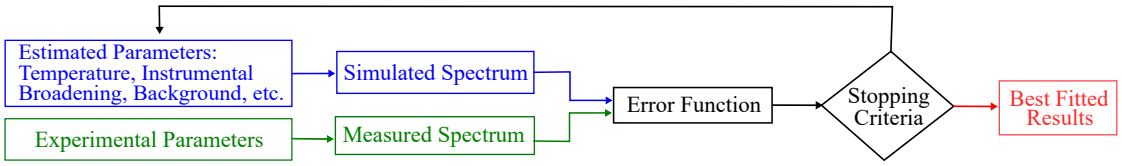

Fig. 3.7 Illustration of the spectral fitting algorithm.

The error function was controlled by the $lsqcurvefit$ function in MATLAB based on a so-called Trust-Region-Reflective algorithm. The optimization process is mainly to find the minimized error function which stands for the deviation of the simulated spectrum from the measurement. The optical depth $\tau = -\ln \frac{I_t}{I_0}$ of both the measured and the simulated spectra

were calculated for the comparison. Two spectral fitting methods were used to analyze the measured spectra: directive fitting and second derivative fitting, respectively. For both fitting methods, a constant baseline correction was considered. The instrumental broadening was regarded as a Voigt profile and added as float parameters, due to the fact that the detailed instrumental broadening profile was unknown. It should mention that OH concentration is not available from the fitting results due to the very low OH concentration at the measurement position. Thus both the measured and the simulated spectra were normalized and information about the absolute intensity is not utilized. Other than the normal directive fitting method, the second derivative fitting was also tested because it is found that the temperature is more sensitive to changes in magnitudes and shapes of the absorption lines than baseline errors, while the former method is sensitive to both the magnitudes and the baselines.

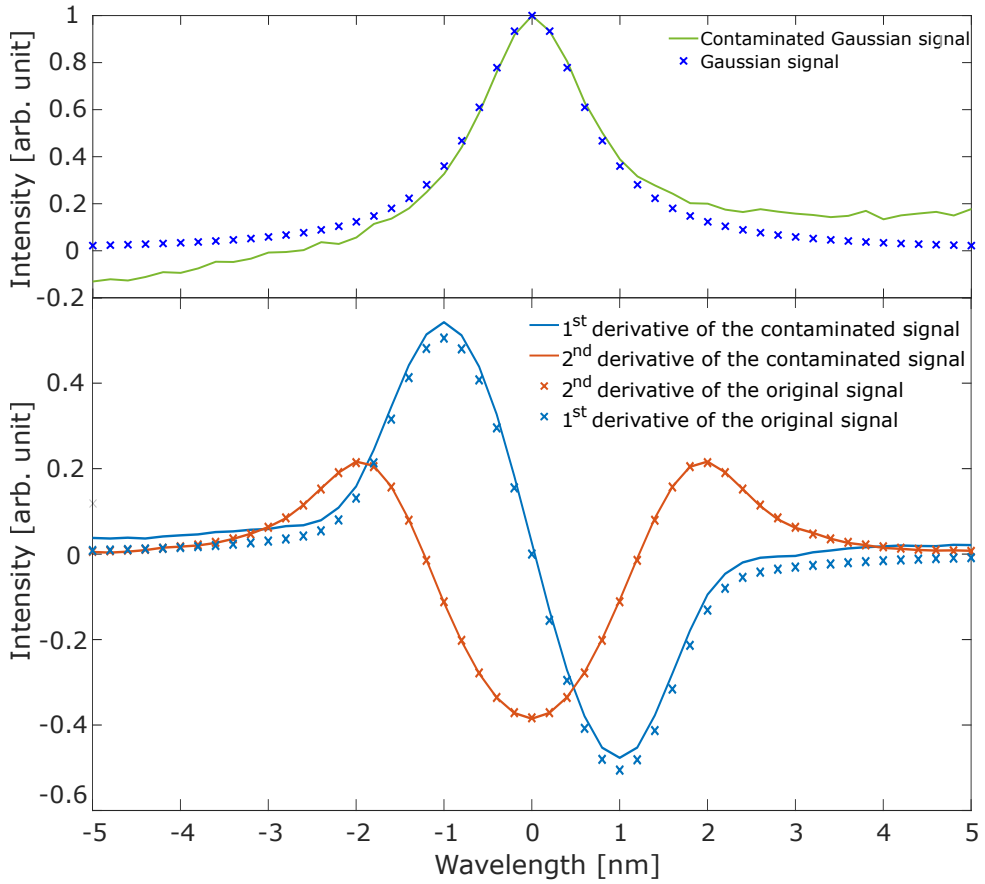

Fig. 3.8 An illustration of the derivative filters. The original Gaussian signal and the contaminated signal are shown on the top. Below are the derivatives of both signals realized by the Savitsky-Golay differentiation method.

In this work, the second derivative of the spectra was implemented by the Savitsky-Golay differentiation method. An illustration of the advantage of the second derivative fitting method is shown in figure 3.8. A Gaussian-shaped signal with a 1.5 nm HWHM was generated for

testing, and the data were sampled with a spacing of 0.2 nm. A random noise signal along with a linear baseline deviation was added to the original Gaussian signal, as represented by the green curve on the top. The first derivative and the second derivate of both the original signal and the noise-contaminated signal are shown in the lower part of figure 3.8. The derivatives were achieved by the Savitsky-Golay differentiation method using a third order polynomial with a frame length of 19. It can be seen from the figure that both derivatives of the contaminated Gaussian signal to some extent reduce the deviations caused by the linear baseline error and the random noise signal. Nevertheless, the first derivative is still a little bit out of the original shape, while the second derivative is almost free from the baseline deviation and the noise signal.

Chapter 4

Results and discussion

The experimental results are presented in the following sections. Firstly, TLAF temperature measurements for different flame cases are described. Secondly, the results of the two-line alkali emission method are presented. Thirdly, the measured OH absorption spectra and best-fitted results are discussed. A comparison of the thermometric methods involves in the work is given in the end.

4.1 Temperature evaluation by TLAF

In this section, temperature of hot gas in six series of flames were measured. The fluorescence distributions of indium atoms along the long side of the burner are shown in figure 4.1, and the corresponding temperature distribution is shown in figure 4.2. The seeding of indium atoms in the flame is not perfectly homogeneous as expected. Nevertheless, as a ratio-metric thermometric technique, the derived temperature is not influenced by the uneven indium distribution. The temperature measurements were conducted 5 mm above the burner outlet; at this position, the temperature was homogeneously distributed within a horizontal distance of more than 70 mm. The distribution of hot gas temperature around the border parts of the burner is much lower due to the cooling effect of the surrounding air.

The environment of hot gas was provided by several premixed flames with different temperature and excess oxygen, as shown in table 4.1. Four temperature series of flame cases were investigated; each has five oxygen cases with oxygen contents varied from 0.7% to 6.4%. Another two temperature cases with 3.8% O_2 were also studied for the purpose of supporting the following two-line alkali emission method. The flow rates and the oxygen contents of these

flames are presented in the table, along with the temperatures derived from TLAF measurements. For each temperature measurement,50 groups of fluorescence signals were recorded, and a curve of temperature distribution was determined. The final result gives the average temperature within the homogeneous region of the curve, which corresponds to the horizontal distance from -35 mm to 35 mm.

For flame series T1 $\sim$ T4, the temperatures were measured from O3 cases. The temperature variation among different oxygen cases is considered as negligible due to the identical jet-flow rates as well as the same total co-flow gas rates. The temperature difference caused by the change in ratios between N_2 and air in this work is estimated to be less than 15 K.

In addition, it should be mentioned that most flame cases were measured with the seeding of $InCl_3$ water solution, but the temperature of T4 was measured with the seeding of TMI. The difference in seeding methods does not affect the evaluation result, but it does affect the distribution of indium atoms. The measured distributions of fluorescence signals and hot gas temperature along the long side of the burner are shown in figure 4.3. When using TMI seeding, the indium atoms are most likely to stick on the walls of the jets, resulting in an uneven distribution of the signals. Nonetheless, the temperature distribution is not affected by the uneven distribution of indium atoms, and the burner still shows good spatial uniformity.

The precision of this temperature measurement can be seen from figure 4.2 and 4.3. There are also some systematic errors that are hard to detect but affect the accuracy of this method. Firstly, the inaccurate value of the Einstein A coefficients, which according to [41] causes a temperature error of about 2% at 1800 K. Secondly, the instrumental errors, including the erroneous calibration of laser power, the non-linear response of the camera, and the instability of the lasers. The inaccuracy in spectral line shape simulation would also be a source of systematic error. Generally speaking, the uncertainty of temperature measurements are estimated to be $\pm$ 50 K.

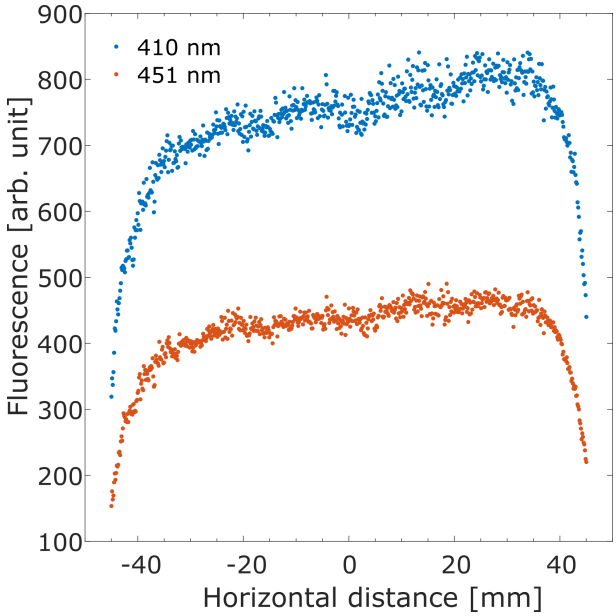

Fig. 4.1 The radial distributions of the indium LIF signals in the burner. Indium atoms were seeded from $InCl_3$ water solution in the form of fog. Both signals are centering at the wavelength of 451 nm, while the blue one and the orange one were pumped by the 410 nm laser and the 451 nm laser, respectively. The results show an average of 50 images.

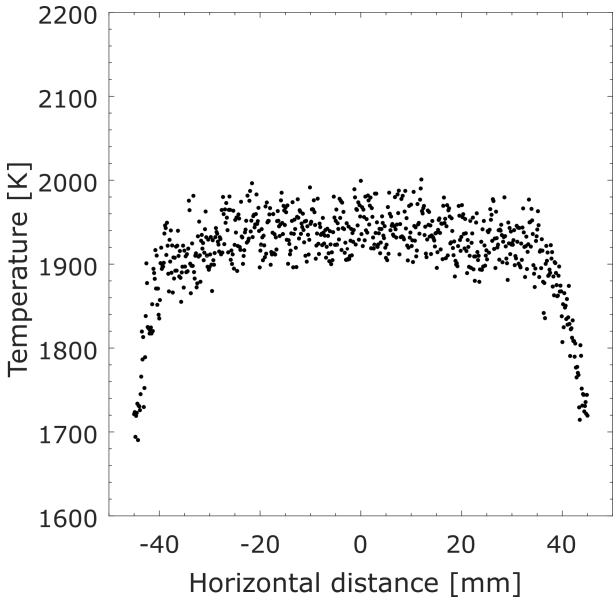

Fig. 4.2 The horizontal temperature distribution measured by TLAF method. Experiments were conducted 5 mm above the burner outlet. The length along the long side of the burner outlet is 100 mm, where four asbestos plates ($\sim$ 3 mm) were added to reduce the heat loss. This image shows an average of 50 individual temperature measurements, and the average temperature within the homogeneous region is determined to be 1935 K.

Table 4.1 Flow rates (298 K and 1 atm) and the measured temperature of studied flame cases.

Flames	Jet-flow (L/min)			Co-flow (L/min)		O_2 in burnt gas (%)	Oxygen case	Measured Temperature (K)
	CH_4	Air	O_2	N_2	Air			
Series T1	2.6	13.16	2.71	29.7	0.3	0.7	O1	1695
				26.2	3.8	2.2	O2	
				22.5	7.5	3.8	O3	
				18.2	11.8	5.7	O4	
				16.5	13.5	6.4	O5	
Series T2	2.8	18.65	1.98	20.0	0.0	0.7	O1	1935
				16.8	3.2	2.2	O2	
				12.7	6.3	3.8	O3	
				9.6	10.4	5.7	O4	
				6.5	13.5	7.2	O5	
Series T3	3.1	20.65	2.19	15.0	0.0	0.8	O1	2090
				12.2	2.8	2.2	O2	
				9.2	5.8	3.8	O3	
				5.5	9.5	5.7	O4	
				2.5	12.5	7.2	O5	
Series T4	3.4	22.65	2.40	12.0	0.0	0.9	O1	2150
				9.5	2.5	2.2	O2	
				6.3	5.7	3.8	O3	
				2.7	9.3	5.7	O4	
				0.0	12.0	7.2	O5	
T5	3.0	20.00	2.12	11.7	6.3	3.8	O3	2010
T6	3.8	25.32	2.68	6.0	6.0	3.8	O3	2240

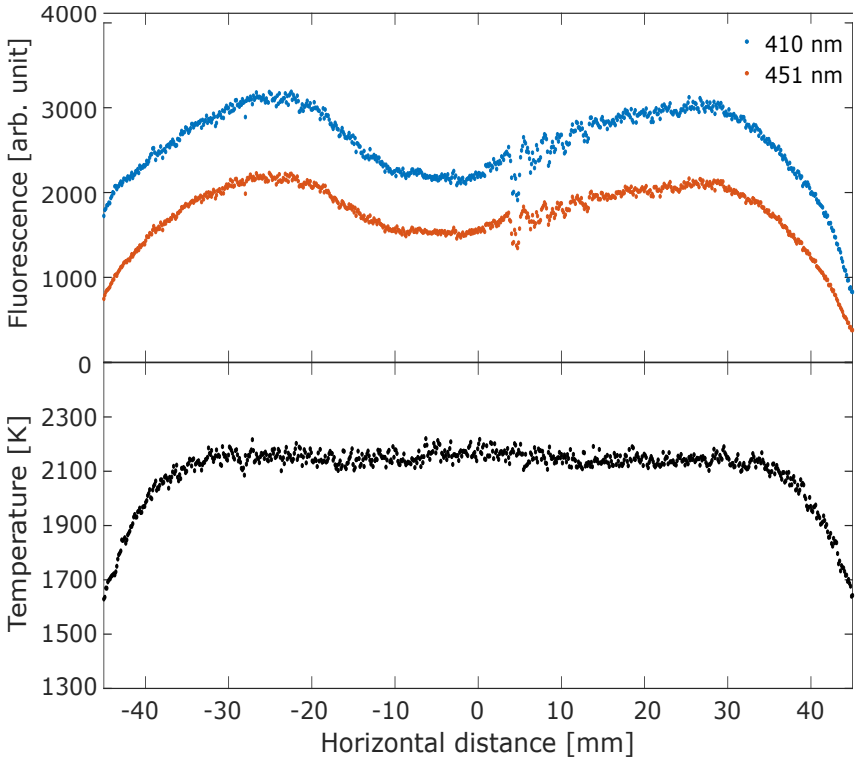

Fig. 4.3 The horizontal distribution of fluorescence signals and the corresponding temperature derived from TLAF method. Measurements were conducted 5 mm above the burner, with the flame T4, and the indium was seeded into the flame from the specially designed TMI bubbler. The hot gas temperature of this case is determined to be 2150 K.

4.2 Two-line alkali emission method

In this section, the emission spectra of atomic Na and K are investigated to find the relationship between the emission intensity ratios and the temperature of the hot gas. The temperature dependence of the intensity ratios between Na doublets at 589 nm and K doublets at 766 were studied. Most of the results presented in this section belong to this part. The ratios between potassium 404 nm emission lines and 766 nm emission lines were also tested to see potential temperature dependence. Nevertheless, as will be presented in the following contents, no promising results were obtained from this attempt.

The spectrometer is not used in the measurement of alkali emissions, instead, an ICCD camera mounted with a stereoscope and two bandpass filters were adopted. Three bandpass filters were involved in this work, centering at 404 nm, 589 nm, and 766 nm, respectively. The filters have a HWHM of about 5 nm, which is much larger than the wavelength difference of the alkali doublets involved in this experiment, as presented in table 3.2 in section 3.3. Therefore, the camera captured signals of both emission lines through each filter. Nonetheless, in the calculation of the emission intensity ratios, the Na and K doublets was treated as single emission lines. The error induced by this approximation is no more than 1%, as can be derived from mathematical computations. In the following content, the potassium doublet measure by the 766 nm bandpass filter is sometimes expressed as the emission lines at 766 nm, and this includes both the 766.49 nm and the 769.90 nm spectral lines.

4.2.1 Two-line emission method: Na/K

Before investigating the temperature dependence of alkali emission ratios, the influence of self-absorption was studied at first. As previously mentioned, the re-absorption of the emitted light to some extent reduces the intensity of the outgoing light, and this effect is dependent on numerous factors, including transition wavelength, the concentration of the alkali atoms, the Einstein A coefficient, the spectral line shape, etc. It is difficult to precisely calculate the fraction of re-absorbed light because the concentration of Na atoms in the hot gas was not experimental determined. Though it is possible to get concentration information from CHEMKIN simulation, the results are not accurate enough to be directly put into mathematical calculations.

The ratios of Na/K emission intensity measured at different atomic concentrations are shown in figure 4.4. The concentration of K atoms, as measured by the TDLAS method,

was adjusted by changing the flow rate of the seeding gas. To avoid the influence of high self-absorption, the atomic concentration was in the range of several parts per billion (ppb) particles. According to chemical simulation, the concentration ratio between atomic Na and K is decreasing with the increase of temperature. To assure the highest Na concentration was covered, the data were measured in the hot gas with the second lowest temperature case T2. The T1 case was not adopted due to the poor signal-to-noise ratio in this concentration range, which is about 25 times lower than that of T2. The concentration of the Na atoms at equilibrium state is proportional to the K atoms by a fixed factor according to the simulated results by CHEMKIN. The emission intensity of K is shown by blue dots. The emission intensity of Na is not plotted but shows the same increasing trend with that of K. The intensity ratios between the emission intensity of Na and K are changed within a range of 3% with the increase of atomic concentration, which is acceptable within the experimental error range. In the following measurements, the concentration of atomic K was monitored by the TDLAS and controlled to be in the range of $3 \sim 5$ ppb, where the intensity ratios Na/K were nearly constant, and the influence of self-absorption can be ignored.

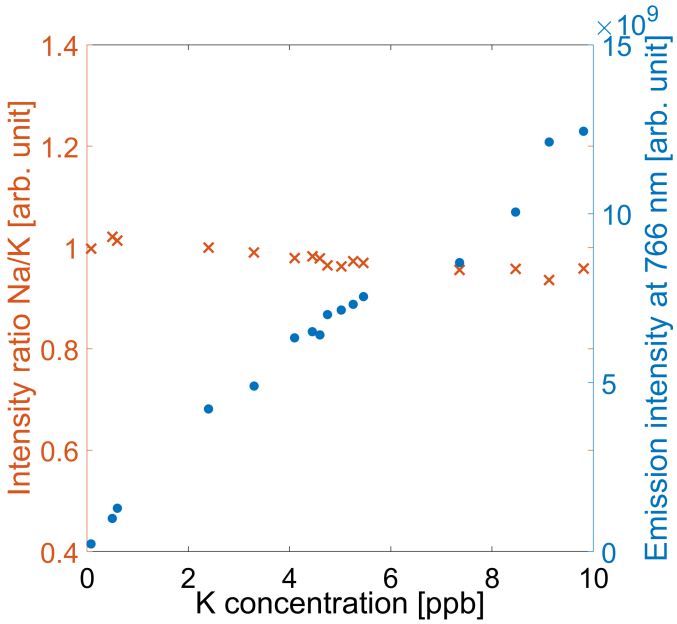

Fig. 4.4 Concentration dependence of K emission intensities and the Na/K intensity ratios. The thermal emissions were measured from the hot gas provided by flame T2O3.

The results of the temperature dependence are shown in figure 4.5. Intensity radios measured under different oxygen conditions are marked by different symbols, corresponding to the flame cases described in table 4.1. The emission intensity ratios at O1 oxygen cases strongly deviate from the others, which might result from the very high chemical reactivity at low

oxygen content comparing to the other cases. According to [31], the effect of supra-thermal chemiluminescent excitation will cause a overpopulation in low-temperature near stoichiometric flames, especially for potassium, and this could to some extent explain the deviation at low oxygen cases. Other than O1, the results at the other four oxygen cases are not strongly influenced by the oxygen content. The mean values of the other four oxygen cases at different temperature are exponentially fitted and represented by the blue dash line. The fitting result is expressed by:

$$R = 17.26 \times \exp\left(-\frac{7287}{T}\right) + 0.5481,$$

where R stands for the ratio between Na emission intensity and K emission intensity, T is the temperature of the hot gas. The coefficient of determination r^2 equals to 0.9961.

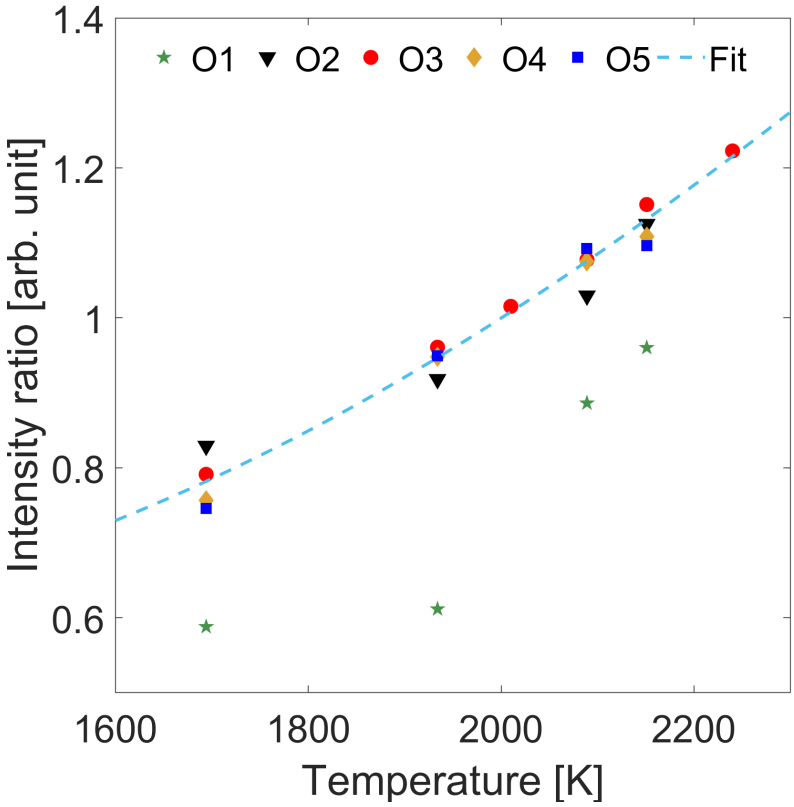

Fig. 4.5 Measured Na/K intensity ratios at several different temperature and oxygen conditions. The ratios measured at O1 conditions, as marked by pentagrams, are clearly out of line due to the low oxygen contents. The average ratios of the other four oxygen conditions at different temperatures are exponentially fitted and shown by the dashed line. Each data shows an average of 100 images.

Figure 4.6 shows the fitting results of all O3 measurements in comparison with the aforementioned fitting result of the average of the measurements O2 $\sim$ O5. The fitting equation of

the red curve is

$$R = 14.65 \times \exp\left(-\frac{6842}{T}\right) + 0.5334,$$

with a r^2 of 0.9984. Both the O3 fit curve and the average fit curve indicate that the Na/K intensity ratio is to some extent related to the temperature of the hot burnt gas, and the temperature can be determined from the empirical curves under certain conditions. The precision of the measurement is roughly 5%, as shown in figure 4.5 and 4.6. The experimental error at T1 is larger than that of the higher temperatures due to the bad signal-to-noise ratio and probably the existence of chemi-excitation.

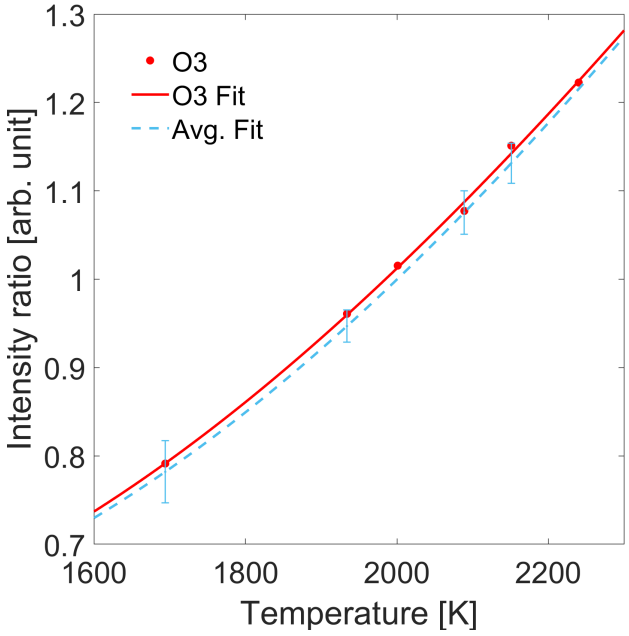

Fig. 4.6 Fitted curves of Na/K intensity ratios as a function of temperature. The red line represents the fitting curve of all O3 results. The dash line represents the fitting result for the mean values of O2, O3, O4, and O5 measurements.

Comparing with the expression of the emission radiance ratio (equation 2.11) presented in section 2.2.2, where the exponential term $\exp(\frac{E_{q,2} - E_{q,1}}{kT})$ equals to $\exp(-\frac{5659}{T})$ (cf. table 3.2 in section 3.3), the experimental emission ratios increase slower with the temperature. This mainly attributes to the Na/K equilibrium concentration difference at different temperatures. As aforementioned, the ratio of equilibrium concentration Na/K is decreasing with the increase of temperature, and thus the measured emission ratios are lifted at low temperatures, making the experimental curves to be flatter.

The error sources of this measurement also include the errors in the TLAF temperature measurements as well as some other experimental errors. Firstly, the angles of view of the

stereoscope from the two filters are not totally overlapped. Although the signals of Na and K were selected from the same region above the burner, the transmit directions of the collected light were slightly changed, which will lead to a difference in the measurement of radiance. Secondly, during the measurement, the burner heated up gradually with time, and hence the temperature of the hot gas was also slowly increased. As a result, the actual gas temperatures might somewhat deviate from the temperatures measured by the TLAF method. That the camera was not always working in the linear-response region would be another possible error source. The temperature deviation from the TLAF results is estimated to be less than 2%, and the total error of the measurement is estimated to be $\sim$ 4%. Considering also the uncertainty of $\pm$ 50 K of the temperature measurement, the uncertain of this two-line emission thermometry is conservatively estimated to be $\pm$ 100 K.

4.2.2 Test: emission intensity ratio of potassium between 404 nm and 766 nm

The emission intensity ratios between K doublets at 404 nm and 766 nm were tested to see if it can be used to deduce temperature. However, the ratios are strongly dependent on the concentration of K atoms, as shown in figure 4.7, which suggests that it is not suitable to be selected as temperature indicators.

In this measurement, the K concentration was adjusted from roughly 1 ppb to 10 ppb but not quantitatively measured; instead, the K concentration could be somewhat inferred from the emission intensities at 766 nm. As mentioned, the intensity ratios increase rapidly with the increase of concentration, and the variation is larger than that caused by the change in temperature. The possible reasons for the in-feasibility of this method are discussed as follows.

Firstly, most of the emission light at 404 nm might be excited by chemical reactions, where the Boltzmann distribution law is no longer in force. This overpopulation can be proofed by the measured emission intensity ratios between 404 nm and 766 nm. According to the Boltzmann distribution law, the ratio of the thermal emission intensities is quantitatively determined at a certain temperature due to the common ground state, as expressed by equation 2.11 in section 2.2.2. The theoretical ratio is $\sim 1.3 \times 10^{-5}$ at 2000 K, which is much smaller than the experimental result. Considering the attenuation of the ND filter as well as the quantum efficiency of the ICCD camera, the measured intensity ratio is of the magnitude of 10^{-4}, and as a result, the overpopulation of the 5p excited state is most probably caused by chemi-excitations.

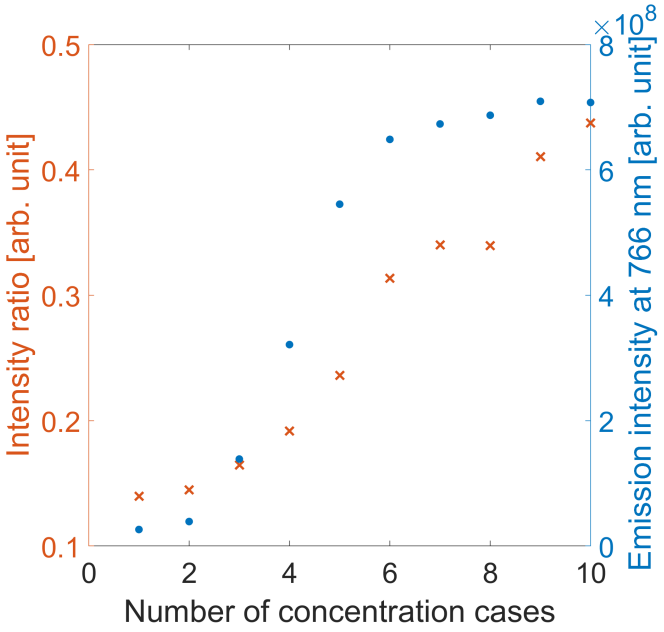

Fig. 4.7 The measured intensity ratios between the potassium 404.4 nm, 404.7 nm emission lines and the 766.5 nm, 769.9 nm emission lines at different K concentration cases with the flame T2O3. The emission intensity of the latter spectral lines is represented in the right y-axis, which was measured with an ND 9 filter. The x-axis shows the number of different K concentration cases with the concentration ranging from approximately 1 ppb to 10 ppb.

Secondly, besides potassium, other molecules and atoms also have spectral lines in the wavelength range that can be transmitted by the 404 nm filter. It has been found that the emission signals from the hot gas background without seeding fog were even stronger than that from the K atoms. Accordingly, a slight fluctuation of the flame would cause a big influence on the measurement of K emissions. During the measurement, the background images and the images with alkali seeding were captured in succession, and this would introduce errors in the background subtractions.

4.3 Temperature determination from OH absorption spectroscopy

The full spectrum measured by the broadband UV absorption and the best fit are shown in figure 4.8. It can be seen that the fitting result is acceptable in the middle but shows evident wavelength shifts at both ends of the spectrum. The wavelength shift comes from the sine-shaped dispersion relation of the Czerny-Turner spectrograph involved in this measurement, which is dependent on various parameters, such as the groove spacing of the dispersion grating, the pixel spacing of the detector, the operating diffraction order, and the diffraction angle of the first pixel. It is usually hard to accurately determine the values of these parameters since they change with the specific optical configurations and might be influenced by other factors due to the thermal expansion and potential mechanical creep of the hardware. For this reason, the wavelength shift of the measured spectrum was not corrected, instead, the center part from 307.7 nm to 311.2 nm was extracted for the following temperature evaluations.

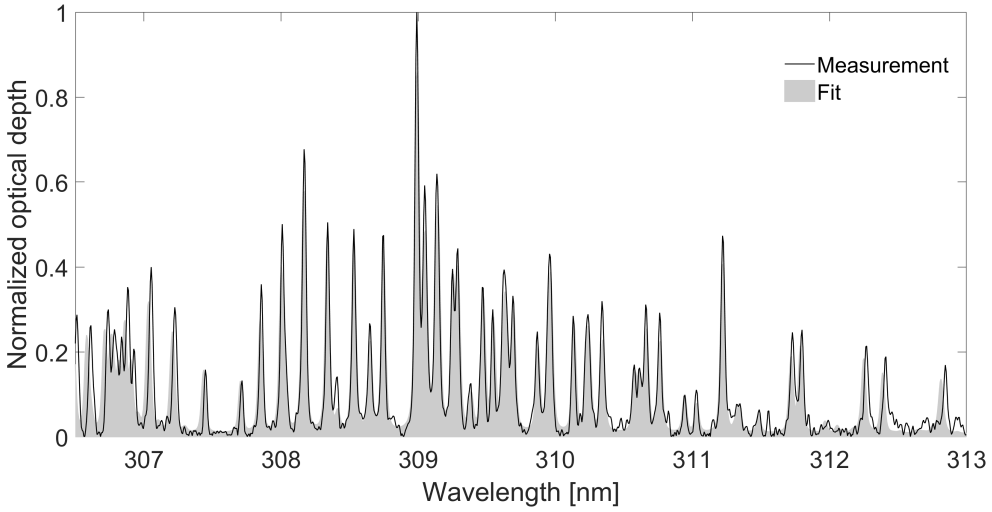

Fig. 4.8 Measured spectrum and the best fit. The instrumental broadening were treated as floating parameters, and the temperature simulated in this fit is 1489 K.

The result of the extracted spectrum by the direct fitting method is shown in figure 4.9, along with the fitting residual. Figure 4.10 shows the sum of squared difference as a function of simulated temperature. For each temperature, the instrumental broadening, magnitude, and the zero-order baseline correction coefficient are treated as floating parameters to match the measured spectrum. The best fit temperature is marked by the red triangle, which corresponds to 1420 K. It can be seen from figure 4.9 that with a temperature of 1420 K most data points are

appropriately fitted, and the fitting residuals are evenly distributed. Still, some of the peaks are distinguished with the fitting result, and the fluctuations of the baseline in measured spectrum somewhat influence the fitting result. As mentioned in chapter 3, no baseline correction was conducted before the fitting procedure, as it is found that the baseline errors can be properly eliminated by using the second derivative fitting method.

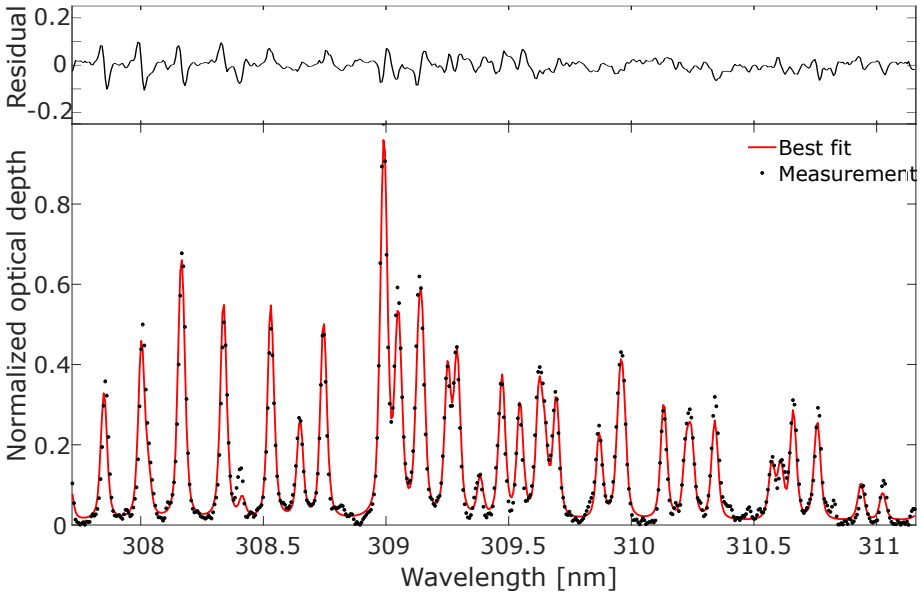

Fig. 4.9 Best fit of measured spectrum by direct fitting along with the fitting residual. The instrumental line shape is estimated as a Voigt profile, with a Lorentzian HMHW of 1.49 cm^{-1} and a Gaussian HMHW of 2.10 cm^{-1}, and the evaluated temperature is 1420K.

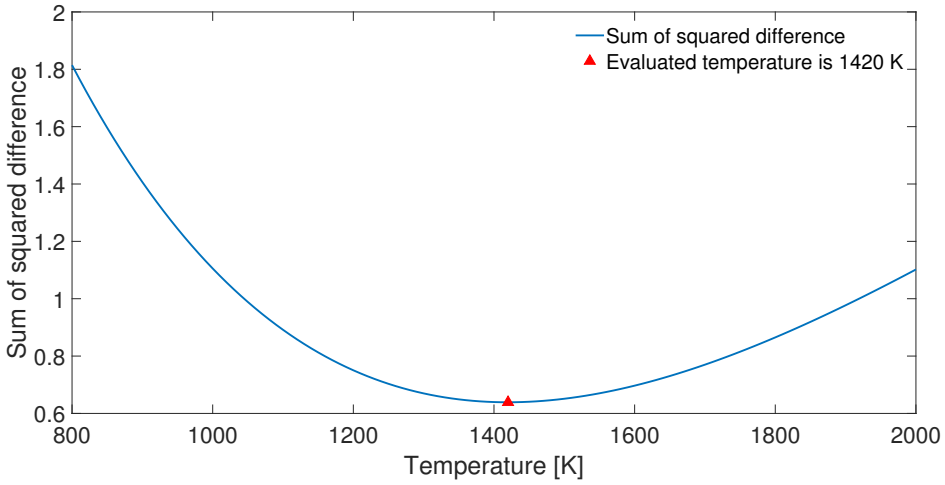

Fig. 4.10 The sum of squared difference at different temperature for the direct fitting method. The red triangle marks the position of the inferred temperature.

The spectral fitting result by using second derivative method is shown in figure 4.11. In this method, the simulated spectra were re-sampled at the same sampling wavelengths as the

measured spectrum for the post-processing procedures. As aforementioned, an instrumental broadening with a Voigt profile was applied in the simulated spectrum. Comparing with figure 4.9, more simulated data points are in consonance with the measurement, and the fitting residual is oscillating evenly below and above zero with no obvious drift to either side. The fitting residual tends to smaller toward the longer wavelengths, and this is to be expected because the emission intensity of the UV lamp is stronger at longer wavelengths and decreases as the wavelength decreases across the vibrational band. The relative intensity of noise signal is inversely proportional to the emission intensity of the light source and thus can be expected to cause larger residuals at shorter wavelengths. In addition, the correction of wavelength shift performs perfectly in the middle and at higher wavelengths but shows partially deviations at lower wavelengths.

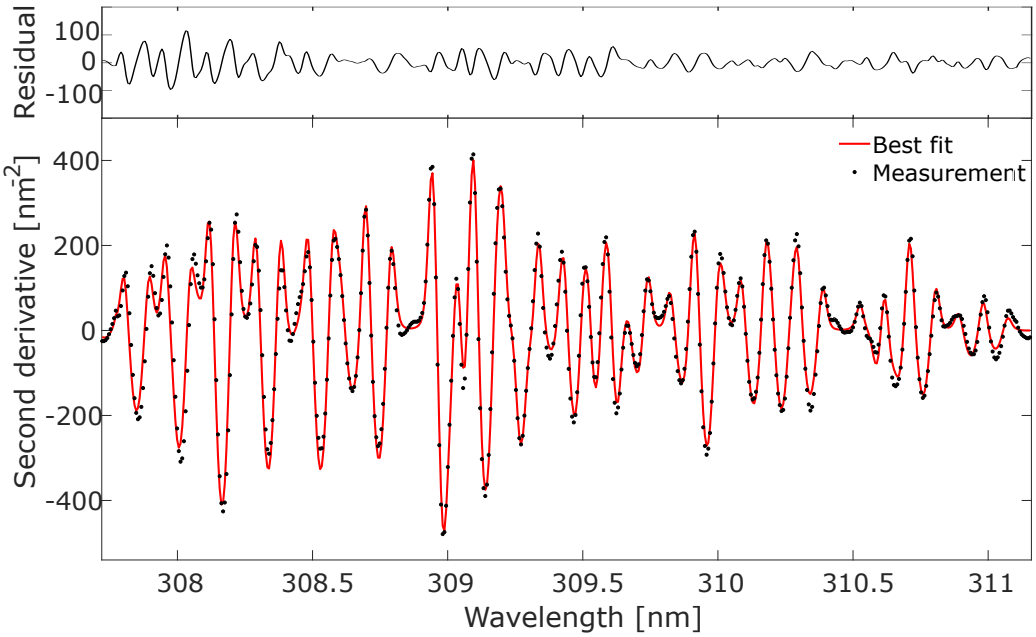

Fig. 4.11 Best fit of measured spectrum by second derivative fitting along with the fitting residual. The second derivative of the spectra was realized by Savitsky-Golay differentiation method using a moving window size of 17 data points and a polynomial order of 3, which can provide with a satisfactory frequency response and meanwhile avoid excessive noise amplification. The instrumental line shape is estimated as a Voigt profile, with a Lorentzian HMHW of 1.30 cm^{-1} and a Gaussian HMHW of 2.31 cm^{-1}. The derived temperature is 1466K.

The variation of the sum of the squared difference of the inferred measurement using the second derivative fitting with temperature is shown in figure 4.12. Comparing with figure 4.10, the valley of the curve apparently shifts to a higher temperature region, and the evaluated temperature by the second fitting method is 1466 K.

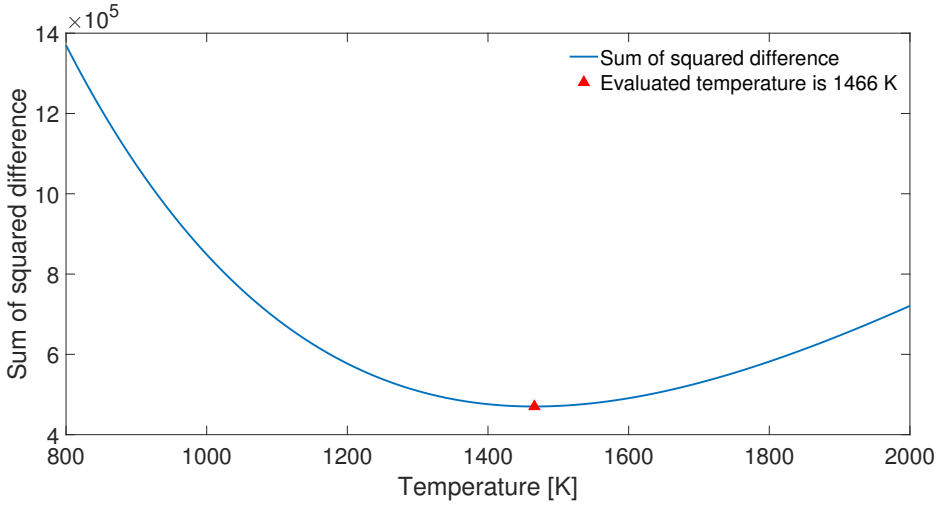

Fig. 4.12 The sum of squared difference at different temperature for the second derivative fitting method. The red triangle marks the position of the inferred temperature.

The best fit result of the direct absorption fitting method was refitted by the second derivative fitting method, and the fitting residual is compared with the best-fit residual of the latter method, as shown in figure 4.13. The fitting residual of the direct fitting result is generally larger, especially in the middle where the peaks of the absorption profile are not appropriately fitted. The second derivative fitting is more sensitive to subtle changes in shapes and magnitudes of the absorption profile, and tolerates larger residuals of the optical path connected with spurious baseline fluctuations. The wavelength shift of the measured spectrum can be determined more accurately to provide better-evaluated parameters in this measurement.

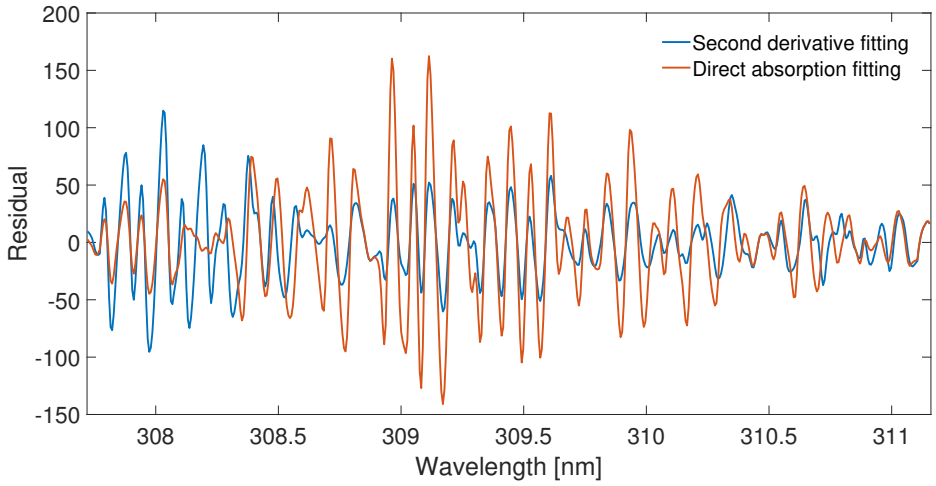

Fig. 4.13 A comparison between the second derivative fitting residual of the direct best fit and the second derivative best fit.

The hot gas temperature was simulated using the GRI-Mech 3.0 [42] in CHEMKIN, resulting in a temperature of $\sim$ 1500K under the assumption of adiabatic conditions. It was also measured by TLAF technique and thermocouple [10], giving results of $\sim$ 1460 K and $\sim$ 1480 K, respectively. Since the flame was not perfectly adiabatic, both fitting approaches in this work evaluated the hot gas temperature fairly well within an error range of 60 K, and the evaluated result of the second derivative fitting method is closer to the temperature measured by TLAF as expected. Still, there are some differences between the simulation and the measurement, for which the possible reasons are discussed here. Firstly, the measured spectrum might not be best described by the simulation. The instrumental broadening was expressed by a Voigt profile in the simulation. However, it depends on optical properties of the equipment as well as the specific optical configuration, and usually cannot be described simply by a Voigt line shape. Secondly, the experiment was conducted 2 mm above the shielding ring of the burner, corresponding to roughly 20 mm above the flame front. The mole fraction of OH decreases rapidly with height above burner, and at the measuring position the OH mole fraction is expected to be in the magnitude of 10 ppm. At this low concentration, the noise caused by the instability of the light source and flame fluctuations would somewhat influence the fitting of the measured OH absorption spectrum, especially the direct absorption fit. Lastly, the fitting residual caused by unevenly distributed wavelength shifts is not neglectable. A wavelength correction algorithm is needed to achieve higher-precision results for both spectral fitting methods.

4.4 Comparison of the thermometric methods

A comparison of the three thermometric method involved in this thesis work is shown in table 4.2. Among them TLAF thermometry is a developed laser-based diagnostic method and is treated as the most accurate method in this work. This method is independent of gas composition, and it is able to provide spatially resolved measurement. However, it requires the introduction of indium atoms, which to some extent limits the application of this technique. Comparing with the TLAF method, the other two thermometric methods are simpler and easier to operate. The measurement of emission and absorption spectra requires less professional skills, and no laser light source is needed. Although there are still some limitations for these two method as listed in table 4.2, they both have considerable advantages under certain conditions.

Table 4.2 Comparison of the advantages and disadvantages of the thermometric methods.

	Two-line atomic fluorescence thermometry	**Two-line alkali emission thermometry**	**Thermometry using OH UV absorption**
Advantages	• Spatially resolved measurement • Excitation wavelengths in the visible spectrum • Strong fluorescence signals • Independent of gas composition	• Emission spectra are acquired quickly • Provides spatially distribution （2-D） • Na and K are widely exist • Easy to operate	• Available for quantitative analysis • Low-cost light source (UV lamps or UV LEDs) • Calibration-free
Disadvantages	• Introduction of atomic species • Complicated excitation scan • Some requires calibration	• Effect of self-absorption in optical thick flames • Requires calibration • Limitation for oxygen concentration	• Requires homogeneous flame • No spatial and temporal information • Possible interferences and absorption from other molecules

For example, it is possible to measure the temperature distribution in a two-dimensional space in the two-line alkali emission method, and no calibration procedure is involved for temperature measurement using OH absorption spectroscopy.

Chapter 5

Summary and outlook

The work reported in this thesis involves three thermometric approaches for flame temperature measurements. Firstly, the hot flue gas temperatures were measured using the TLAF method from the LIF signal of indium atoms. The measured temperature was homogeneously distributed on the multi-jet burner despite of the uneven distribution of indium atoms. The uncertainty of this technique was estimated to be $\pm$ 50 K. The results given by the TLAF measurements were used to test the two-line emission method. The temperature dependence of the ratio of Na/K emission intensity was studied in flames with different oxygen contents. The ratios were found to be increasing with the temperature increase and nearly independent on the oxygen concentration when the oxygen content in the burnt gas is higher than 2.2%, indicating that the effect of chemical reactions can be ignored. Therefore, this method can be used to evaluate temperature at lean conditions, with an estimated uncertainty of $\pm$ 100 K. The emission intensity ratios between the 404 nm lines and the 766 nm lines of K were also studied in this work. Nonetheless, the ratios depended strongly on the K concentration in the measured concentration range and thus were not suitable to be used as temperature markers. In the end, the feasibility of thermometry using broadband OH absorption spectra was examined using the direct fitting method and the second derivative fitting method, leading to inferred temperatures of 1420 K and 1466 K, respectively. The second derivative fitting method is recommended due to the larger tolerance of optical depth residuals when spurious baseline deviations are involved.

Except for the TLAF measurement, no laser is needed in the other two thermometric approaches. Compared to the expensive laser-based thermometric methods, they are cheaper, easier to operate, and also reliable, and thus will have valuable applications in different com-

bustion studies. Still, more research is needed to further optimize these thermometric methods. In the two-line emission method, the concentration of Na atoms could be experimentally determined so that the theoretical relationship between the Na/K intensity ratio and the temperature can be quantitatively validated, and the effect of self-absorption will also be able to quantitatively studied. Then the concentration range where the effect of self-absorption is neglectable can be well defined. In addition, the fraction of excited state alkali atoms excited by chemical reactions can be directly measured by absorption spectroscopy, and the results of the measurements can be used to validate the equilibrium concentrations simulated by CHEMIKIN. For the thermometric approach using OH absorption spectra, only one flame was studied in this work, and more measured spectra are required for a better development of this method. Furthermore, the correction of the non-linear wavelength shift is needed in the future. This can be accomplished either by fitting spectral peaks to the theoretical values or by adding floating parameters to find the exact dispersion relations for the spectrograph. The line shape of the instrumental broadening can also be experimentally determined to improve the precision of this method. A high-precision spectral fit will provide not only an accurate temperature but also information about the OH concentration in hot flue gases.

Acknowledgements

I would like to express my sincere appreciation to my supervisor, Associate Professor Zhongshan Li, for providing me the opportunity to study here with such an attractive task and always being supportive. Special thanks go to Wubin for all the discussions, lab instructions, and patient explanations to my stupid questions. It has been a great honor to conduct my thesis project at Combustion Physics and work together with many amazing people. They have offered much more than Thursday cakes but also an incredible atmosphere and working environment, and for that I am always grateful.

I would also like to thank all my friends either in Lund or not for the memories we have shared during the year. Thank you, Jojo and Chunyan, for the pleasure and laughter we have shared on our way home.

Thank you, mama and papa. I can never thank you enough for the endless understanding and encouragement. The luckiest thing in my world is that I know you are always there for me, so that I can grow up bravely and stably. You are my heroes, and I will always be your little girl. I love you.

References

[1] PRN Childs, JR Greenwood, and CA Long. Review of temperature measurement. *Review of scientific instruments*, 71(8):2959–2978, 2000.

[2] Dean C Ripple, Dana R Defibaugh, Michael R Moldover, and Gregory F Strouse. Techniques for primary acoustic thermometry to 800 k. In *AIP Conference Proceedings*, volume 684, pages 25–30. AIP, 2003.

[3] Sukesh Roy, James R Gord, and Anil K Patnaik. Recent advances in coherent anti-stokes raman scattering spectroscopy: Fundamental developments and applications in reacting flows. *Progress in Energy and Combustion Science*, 36(2):280–306, 2010.

[4] A Tobias Hartlieb, Burak Atakan, and Katharina Kohse-Höinghaus. Temperature measurement in fuel-rich non-sooting low-pressure hydrocarbon flames. *Applied Physics B*, 70(3):435–445, 2000.

[5] GC Herring, William L Roberts, Michael S Brown, and Peter A DeBarber. Temperature measurement by degenerate four-wave mixing with strong absorption of the excitation beams. *Applied optics*, 35(33):6544–6547, 1996.

[6] Jesper Borggren. Two-line atomic fluorescence for thermometry in reactive flows. 2018.

[7] J. M. Seitzman, R. K. Hanson, P. A. DeBarber, and C. F. Hess. Application of quantitative two-line oh planar laser-induced fluorescence for temporally resolved planar thermometry in reacting flows. *Appl. Opt.*, 33(18):4000–4012, Jun 1994. doi: 10.1364/AO.33.004000. URL http://ao.osa.org/abstract.cfm?URI=ao-33-18-4000.

[8] Michael P. Lee, Brian K. McMillin, and Ronald K. Hanson. Temperature measurements in gases by use of planar laser-inducedfluorescence imaging of no. *Appl. Opt.*, 32(27): 5379–5396, Sep 1993. doi: 10.1364/AO.32.005379. URL http://ao.osa.org/abstract.cfm?URI=ao-32-27-5379.

[9] Normand M Laurendeau. Temperature measurements by light-scattering methods. *Progress in Energy and Combustion Science*, 14(2):147–170, 1988.

[10] Wubin Weng, Jesper Borggren, Bo Li, Marcus Aldén, and Zhongshan Li. A novel multi-jet burner for hot flue gases of wide range of temperatures and compositions for optical diagnostics of solid fuels gasification/combustion. *Review of Scientific Instruments*, 88(4): 045104, 2017.

[11] C Th J Alkemade. A theoretical discussion on some aspects of atomic fluorescence spectroscopy in flames. In *Atomic Absorption Spectroscopy*, pages 73–98. Elsevier, 1970.

[12] J Hult, IS Burns, and CF Kaminski. Two-line atomic fluorescence flame thermometry using diode lasers. *Proceedings of the Combustion Institute*, 30(1):1535–1543, 2005.

[13] Jesper Borggren, Wubin Weng, Ali Hosseinnia, Per-Erik Bengtsson, Marcus Aldén, and Zhongshan Li. Diode laser-based thermometry using two-line atomic fluorescence of indium and gallium. *Applied Physics B*, 123(12):278, 2017.

[14] Lloyd Withrow and Gerald M Rassweiler. Studying engine combustion by physical methods a review. *Journal of Applied Physics*, 9(6):362–372, 1938.

[15] J Reissing, JM Kech, K Mayer, J Gindele, H Kubach, and U Spicher. Optical investigations of a gasoline direct injection engine. Technical report, SAE Technical Paper, 1999.

[16] Michael J Mosburger. *Alkali metal spectroscopy for high-speed imaging of burned gas temperature, equivalence ratio and mass fraction burned in internal combustion engines*. PhD thesis, University of Michigan, 2013.

[17] Yuhe Zhang. Measurements and analysis of atomic emission from atomic li, na, and k seeded in different flames for potential application to temperature sensing. 2017.

[18] Klaus C Lück and Franz J Müller. Simultaneous determination of temperature and oh-concentration in flames using high-resolution laser-absorption spectroscopy. *Journal of Quantitative Spectroscopy and Radiative Transfer*, 17(3):403–409, 1977.

[19] Terrence R Meyer, Sukesh Roy, Thomas N Anderson, Joseph D Miller, Viswanath R Katta, Robert P Lucht, and James R Gord. Measurements of oh mole fraction and temperature up to 20 khz by using a diode-laser-based uv absorption sensor. *Applied optics*, 44(31): 6729–6740, 2005.

[20] Walter R Lempert. Microwave resonance lamp absorption technique for measuring temperature and oh number density in combustion environments. *Combustion and flame*, 73(1):89–98, 1988.

[21] Logan W White and Mirko Gamba. Spectrally resolved measurements of absorption of broadband uv light-emitting diodes by combustion radicals. In *55th AIAA Aerospace Sciences Meeting*, page 0387, 2017.

[22] Stefan Schorsch, Johannes Kiefer, Alfred Leipertz, Zhongshan Li, and Marcus Alden. Detection of flame radicals using light-emitting diodes. *Applied spectroscopy*, 64(12): 1330–1334, 2010.

[23] Christopher J Foot. *Atomic physics*, volume 7. Oxford University Press, 2005.

[24] Colin N Banwell, Elaine M McCash, et al. *Fundamentals of molecular spectroscopy*, volume 851. McGraw-Hill New York, 1994.

[25] Department of Physics and Georgia State University Astronomy. HyperPhysics. http://hyperphysics.phy-astr.gsu.edu/hbase/Bohr.html. Accessed: 2018-03-18.

[26] Sune Svanberg. *Atomic and molecular spectroscopy: basic aspects and practical applications*, volume 6. Springer Science & Business Media, 2012.

[27] K Benuehll. Fundamentals of molecular spectroscopy. 1985.

[28] Spectroscopy/Molecular energy levels. https://en.wikiversity.org/wiki/Spectroscopy/Molecular_energy_levels. Accessed: 2018-03-25.

[29] Iouli E Gordon, Laurence S Rothman, Christian Hill, Roman V Kochanov, Y Tan, Peter F Bernath, Manfred Birk, V Boudon, Alain Campargue, KV Chance, et al. The hitran2016 molecular spectroscopic database. *Journal of Quantitative Spectroscopy and Radiative Transfer*, 203:3–69, 2017.

[30] Alan C Eckbreth. *Laser diagnostics for combustion temperature and species*, volume 3. CRC Press, 1996.

[31] C Th J Alkemade, Tj Hollander, W Snelleman, and PJ Th Zeegers. *Metal vapours in flames*. Elsevier, 2013.

[32] C Theodorus J Alkemade and Roland Herrmann. *Fundmentals of analytical flame spectroscopy*. Hilger, 1979.

[33] Ralchenko Yu. Reader J. Kramida, A. and NIST ASD Team (2018). NIST Atomic Spectra Database version (5.5.2). https://physics.nist.gov/asd. Accessed: 2018-03-08.

[34] Edward Uhler Condon and George Hiram Shortley. *The theory of atomic spectra*. Cambridge University Press, 1951.

[35] Wolfgang Demtröder. *Laser spectroscopy: basic concepts and instrumentation*. Springer Science & Business Media, 2013.

[36] John E Dec and JO Keller. High speed thermometry using two-line atomic fluorescence. In *Symposium (International) on Combustion*, volume 21, pages 1737–1745. Elsevier, 1988.

[37] Ronald Whiddon, Bo Zhou, Jesper Borggren, Marcus Aldén, and ZS Li. Vapor phase tri-methyl-indium seeding system suitable for high temperature spectroscopy and thermometry. *Review of Scientific Instruments*, 86(9):093107, 2015.

[38] Maximilian Lackner. Tunable diode laser absorption spectroscopy (tdlas) in the process industries–a review. *Reviews in Chemical Engineering*, 23(2):65–147, 2007.

[39] Wubin Weng, Qiang Gao, Zhihua Wang, Ronald Whiddon, Yong He, Zhongshan Li, Marcus Aldén, and Kefa Cen. Quantitative measurement of atomic potassium in plumes over burning solid fuels using infrared-diode laser spectroscopy. *Energy & Fuels*, 31(3): 2831–2837, 2017.

[40] Reaction Design. Chemkin-pro release 15131. *Reaction Design, San Diego, CA*, 2013.

[41] Iain S Burns, Xavier Mercier, Maxime Wartel, Robin SM Chrystie, Johan Hult, and Clemens F Kaminski. A method for performing high accuracy temperature measurements in low-pressure sooting flames using two-line atomic fluorescence. *Proceedings of the Combustion Institute*, 33(1):799–806, 2011.

[42] Gregory P Smith, David M Golden, Michael Frenklach, Nigel W Moriarty, Boris Eiteneer, Mikhail Goldenberg, C Thomas Bowman, Ronald K Hanson, Soonho Song, WC Gardiner Jr, et al. Gri-mech 3.0, 1999. *URL http://www. me. berkeley. edu/gri_mech*, 2011.